Princetonlaan 6
3584 CB Utrecht
P.O. Box 80015
3508 TA Utrecht
The Netherlands

www.tno.nl

T +31 88 866 42 56
F +31 88 866 44 75

TNO report

TNO ???

SRIMA: Background Information of the Python Tool

Date March, 2023

Author(s) Peter A. Fokker & Loes Buijze

Copy no
No. of copies
Number of pages 49 (incl. appendices)
Number of appendices
Sponsor
Project name Seal and Reservoir Integrity through Mechanical Analysis (SRIMA)
Project number

Contents

Abstract

We have developed expressions for the fast calculation of temperatures, pressures, and induced poro-elastic and thermo-elastic stresses as a result of the injection of cold fluid. The expressions for flow and induced stresses have been developed for a homogeneous, isotropic layer cake model under radial symmetry. In the injection layer the flow is assumed to be fully developed and temperature transfer is in an advective way. In the bounding seal and base layers the pressure and temperature dynamics are assumed diffusive. Validation of the expressions has been achieved through comparison with finite-difference and finite-element codes for temperature, pressure and mechanical processes around an injection well. The expressions capture the first-order characteristics of the pressure, temperature and stress changes. The resulting expressions have been implemented in a tool, SRIMA (acronym for Seal and Reservoir Integrity Mechanical Analysis) which assesses the occurrence of potential tensile stresses, in order to evaluate the risk of hydraulic fracturing, and the occurrence of shear failure in predefined fault planes. The shear failure potential is translated to ground motions through a deterministic seismic hazard analysis. All calculations can be performed in a stochastic framework, which allows the assessment of failure probabilities.

1. Introduction

The safety of geothermal operations in matrix-type geothermal reservoirs requires that injected water remains in the target aquifer to which it was injected. This implies that the sealing integrity of the seal and underburden must be safeguarded. Hydraulic fracturing is a phenomenon that can breach this integrity. It can break intact formation and create a highly conductive flow path through the seal. Fault reactivation or shear fracturing can have a similar effect as it may induce fault slip and/or seismicity which promotes flow due to dilatancy. In addition, safe operations require the mitigation of seismic events that are large enough to be felt at the surface and can potentially result in damage. The work reported here details the development of a tool targeting the assessment of tensile fractures as a proxy for the risk on tensile fracture creation and hydraulic fracturing, and shear failure as a proxy for the risk on induced seismicity. The tool has been given the name SRIMA, an acronym for Seal and Reservoir Integrity Mechanical Analysis.

Both hydraulic fracturing and fault reactivation depend directly on the in-situ stresses and the pore pressures. The assessment of the risk of integrity issues therefore requires knowledge of the pressure and stress development in the reservoir, the seal and the base.

For geothermal operations, the stress development in the reservoir and in adjacent layers is related to the injection of relatively cold water . Two main phenomena must be incorporated if the stress development is to be assessed. In the first place, injection of water is associated with elevated pore pressures. These alter the total stresses through the effect of poro-elasticity. In the second place, the injected water cools the reservoir and its surroundings. This induces a thermo-elastic change of the total stress. An assessment of the stresses due to the injection of cold water therefore requires a calculation that consists of the following ingredients:

- Estimate of the temperature distribution in and above the reservoir
- Estimate of the pressure distribution in and above the reservoir
- Effect of temperature on the in-situ stresses
- Effect of pressure on the in-situ stresses

Knowledge of subsurface processes is commonly marked by large uncertainties. Additionally, many different operational decisions can be envisaged in specific circumstances, such as changing injection rates, changing temperatures, or cessation of injection operations. Therefore, there is a need for estimation methods which are fast and flexible. Such methods are provided by analytical or semi-analytical means. SRIMA targets such solutions. We have devised semi-analytical expressions for the four ingredients of a stress assessment as described in the previous paragraph. The expressions have been benchmarked and validated using comprehensive numerical modelling software.

The document at hand describes the model choices underlying SRIMA, the semi-analytical expressions based on it, and the results of the validation exercise.

2. Model choices and Mathematical Formulation

SRIMA is a semi-analytical tool that helps the user perform quick mechanical calculations assess the possibility of fault reactivation and hydraulic fracturing. It also supports stochastic analyses to assess the effect of parameter uncertainty. This choice is the background of many following model choices.

2.1. Model geometry, pressure and temperature

2.1.1. Basic assumptions

The tool has been developed for a radially-symmetric reservoir where fluid is injected in a well in its centre (Figure 1). Three layers are present: the permeable layer in which the injection takes place, and the overlying and underlying, low-permeability layers. As a consequence, pressure and temperature fields are also radially symmetric. Injection is supposed to take place evenly over the complete height of the aquifer, and to result in pressure and temperature fields independent of the vertical position in the aquifer. In the aquifer, flow is modelled under steady-state conditions and heat transport is assumed to take place by advection only. In the bounding layers both pressure and temperature are assumed to be controlled by diffusion (Carslaw & Jaeger, 1992; Dake, 1983; Nield & Bejan, 2006). These model choices facilitate the use of analytical expressions for pressure, temperature and stress (Candela, Van der Veer, & Fokker, 2018; Myklestad, 1942; Perkins & Gonzalez, 1985). A (virtual) fault can be defined as a plane at any position and orientation, as long as it is no flow barrier and does not introduce an offset between reservoir parts (see 3.3 on the effect of offset on induced stress changes).

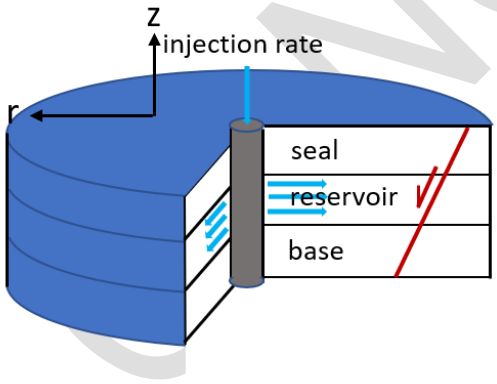

Figure 1 Radially-symmetric geometry used in SRIMA for analysis of thermo- and poro-elastic stresses in a reservoir caused by injection of cold fluids. Injection is assumed to take place over the entire reservoir height.

The radial symmetry comes with limitations. First, anisotropy of the permeability cannot be incorporated. As a consequence, also the temperature profile is radially symmetric. We feel, however, that this still catches the main effect of cooling and pressurization around the reservoir. The induced stresses, although also radially symmetric, do not preclude anisotropy: a virgin stress field that is anisotropic with different values for the minimum and maximum horizontal stress can be incorporated as background field.

A more severe limitation induced by the radial symmetry is that possible offsets between reservoir positions at two sides of a fault cannot be incorporated. Stress concentrations connected to such offsets (Buijze, van den Bogert, Wassing, & Orlic, 2019) are therefore not included. However, when temperature or diffusion to the seal and base is taken into account, these stress concentrations become smoother and the effect of offset on the shear failure potential becomes reduced (section 3.3). For very steep dips (>75°), offset still influences the failure potential. However, most normal faults have orientations less than this, in the order of 60 °.

The second symmetry choice is that pressure increase and temperature change in the injection layer are taken independent of vertical position. For relatively thin and homogeneous layers this approximation is justified: the influence of seal and base on these fields is only limited. For thicker reservoir layers and layers with vertical heterogeneity, the approximation is not always warranted. Heating of the injected fluid in the injection layer may not be distributed over its full height and channeling may cause thinner cooled regions reaching further into the reservoir.

The pressure distribution can be complicated due to the well completion. In the case of a limited perforation interval, the pressures at the upper and lower reservoir boundaries are smaller than at the wellbore; at the perforations they will be larger than calculated because of flow contraction. In the case of a deviated wellbore the temperature distribution will be affected for a short time after starting the injection and affect only the pressure distribution closest to the wellbore. For both cases, the effect on the induced stresses at distances of a limited number of wellbore radii away will be very limited.

Furthermore, geothermal projects typically consist of both an injection and a production well. The effect of the producer on the pressure field around the injector will become sizeable on distances from the injection well which are of the order of the well distance. The cooled volume will develop a drop shape towards the production well (e.g. Figure 34). However, perpendicular to the doublet orientation the radial symmetric assumption of only the injection well will be an adequate approximation (Buijze et al., 2021). Therefore, for a doublet oriented parallel to major fault structures, as most doublets are in the Netherlands, the effect of ignoring the production well on the extent of the cooled volume is minor.

2.1.2. Temperature distribution

Injection into the reservoir involves thermal effects through convection and conduction. The differential equation describing the temperature T reads (Nield & Bejan, 2006).

$$(\rho C)_{\mathrm{rock}} \frac{\partial T}{\partial t} + (\rho C)_{\mathrm{fluid}} \mathbf{v} \cdot \nabla T = \nabla \cdot (K_{\mathrm{rock}} \nabla T) \qquad 1$$

with ρ the density; C the specific heat; $\mathbf{v}$ the superficial fluid velocity; K the heat conductivity. The subscript “rock” refers to the fluid-filled matrix; the subscript “fluid” to the injected fluid. This equation assumes equal temperature of the fluid and the solid where they are in contact.

Mossop (2001) formulated a solution to the diffusion-advection equation in a system with purely radial-horizontal convection in a advection-dominated permeable layer or horizontal fracture, and purely vertical diffusion in the low-permeability overlying and underlying layers. The equations were independently developed by Barends (2010). Candela, Van der Veer, & Fokker (2018) also used this formulation.

The solution for the temperature in the seal, T_{seal}, and in the reservoir, T_{aq}, with layer of thickness h (centered around z=0) in which a relatively cool fluid is injected with a mass injection rate $\dot{m}$ from time t=0 onward reads:

$$T_{seal}(r,z,t) = T_0 + \Delta T_0 \operatorname{erfc}\left[\frac{ar^2 + b\left(|z| - \frac{h}{2}\right)}{\sqrt{t - cr^2}}\right] H(t - cr^2)$$

$$T_{aq}(r,t) = T_0 + \Delta T_0 \operatorname{erfc}\left[\frac{ar^2}{\sqrt{t - cr^2}}\right] H(t - cr^2)$$

$$a = \frac{\pi K_{\mathrm{rock}}}{\dot{m} c_{\mathrm{w}} \sqrt{\kappa_{\mathrm{T}}}}; b = \frac{1}{2\sqrt{\kappa_{\mathrm{T}}}}; c = \frac{\pi h \xi \rho_{\mathrm{fluid}}}{\dot{m}}$$

$$\kappa_{\mathrm{T}} = \frac{K_{\mathrm{rock}}}{(\rho C)_{\mathrm{rock}}}; \xi = \frac{(\rho C)_{\mathrm{rock}}}{(\rho C)_{\mathrm{fluid}}} \qquad 2$$

Here, T_0 is the initial temperature, ΔT_0 is the difference between the initial temperature of the rock and the injection fluid. H is the Heaviside function, r is the radial distance from the wellbore, t is time since the start of injection, κ_{T} is the thermal diffusivity and C_{w} is the heat capacity of the injected water.

For sandstone, κ_{T} typically ranges between 4x10^{-7} m^2/s (Carslaw & Jaeger, 1992) to 1x10^{-6} m^2/s (Grant (2013), p.305). A characteristic sandstone reservoir in the Netherlands has a κ_{T} of 7x10^{-7} m^2/s (from K=2.5 W/(m.K) with ρ=2400 kg/m^3 and C=1500 J/(kg.K)).

The solution in the seal at radial distances close to the wellbore is approximately

$$T_{\mathrm{seal}}(r \approx 0, z, t) - T_0 = \Delta T_0 \operatorname{erfc}\frac{z - \frac{h}{2}}{2\sqrt{\kappa_{\mathrm{T}} t}} \qquad 3$$

2.1.3. *Pressure distribution*

The pressure associated with injection of water into an aquifer depends on a number of parameters: injection rate, time elapsed, aquifer permeability and -height, skin, water viscosity of cold (injected) and warm (reservoir temperature) water, distribution of reservoir properties, well configuration and porosity (Dake, 1983).

In a permeable aquifer, a pressure distortion will quickly propagate into the reservoir and the pressure profile around an injection well will become approximately logarithmic (Dake, 1983). With a diffusivity of typically 0.1 m^2/s for a 10 mD reservoir, one day of injection will already result in a logarithmic pressure profile extending to a radius of more than 100 m. If we have obtained a steady-state pressure distribution with negligible leakage to overlying and underlying layers, with a constant-pressure boundary at a distance r_e,, and constant viscosity μ, the pressure distribution in the reservoir $P_{\mathrm{aq}}(r)$ is given by

$$P_{aq}(r,t) = \begin{cases} P_0 + \dfrac{\dot{m}\mu_h}{2\pi\rho_w k_{aq} h} \ln\dfrac{r_e}{r} & (r > r_c) \\ P_0 + \dfrac{\dot{m}\mu_h}{2\pi\rho_w k_{aq} h} \ln\dfrac{r_e}{r_c} + \dfrac{\dot{m}\mu_c}{2\pi\rho_w k_{aq} h} \ln\dfrac{r_c}{r} & (r \le r_c) \end{cases} \qquad 4$$

P_0 is the original reservoir pressure; $\dot{m}$ the mass injection rate; ρ_{w} the density of the injected water; k_{aq} the permeability and h the height of the injection layer. The radius r_c indicates the thermal front, and is taken as the distance from the well where the temperature has decreased to 50% of the total decrease. The viscosities for the hot and cold reservoir parts are μ_h and μ_c.

Due to the low permeability in the adjacent layers (seal and underburden), the pressure distribution there is not stationary and must by determined through the application of Darcy flow and mass balance. This pressure is also described by a diffusivity equation:

$$\frac{\partial P}{\partial t} = \kappa_{\mathrm{P,z}} \frac{\partial^2 P}{\partial z^2} + \kappa_{\mathrm{P,r}} \frac{\partial^2 P}{\partial r^2} \left(t \geq 0; |z| \geq \frac{h}{2} \right)$$

$$P\left(z > \frac{h}{2}, t = 0 \right) = P_0$$

$$P\left(z = \frac{h}{2}, t \right) = P_{\mathrm{aq}}(r) \qquad 5$$

The hydraulic diffusivity $\kappa_{\mathrm{P}} = \frac{k_{\mathrm{seal}}}{\phi \mu c}$ in which k_{seal} is the permeability; ϕ the porosity; μ the viscosity and *c* the compressibility. The value may be different for horizontal and vertical directions due to permeability anisotropy. A very small permeability of 0.00003 mD = 30 nd = 3×10^{-20} m^2 (viscosity of 1 cP; porosity of 10%) already results in a diffusivity of 6×10^{-7} m^2/s, comparable to the value of the thermal diffusivity. This solution is not valid in the case of relatively large permeability in the bounding layers above and below. More research should be performed to formulate a threshold for that value, but we think a ratio between the reservoir and the bounding layers of 10^{-4} should be sufficient in most cases.

In contrast to thermal diffusion, a simple 1D diffusion into seal and base will not work for the pressure. The reason is the large variation of the pressure close to the well. Pressure that is induced in the seal near the well bore will “leak away” both vertically and horizontally, and the second term in the pressure diffusion equation cannot be discarded. Alternatively one can state that the pressure in the seal at some distance is influenced by an extended pressurized area of the reservoir. We therefore adopted an equation similar to the expression for temperature but with the temperature substituted by an effective pressure for such a cylinder in the reservoir. The size and the pressure of the cylinder have been benchmarked with the numerical validation calculations.

$$P(r, z, t) = P_0 + \left(P_{aq}(r, t) - P_0 \right) \operatorname{erfc} \frac{z - \frac{h}{2}}{2\sqrt{\kappa_{\mathrm{P}} t}} \qquad 6$$

For the diffusivity in the seal and the base we take the value as calculated for the virgin reservoir temperature. This will result in an overestimate of the pressure close to the well and close to the interface.

2.2. Mechanical model

2.2.1. Basic assumptions

Induced stresses are calculated with approximations for linearly elastic material, including poro-elasticity and thermo-elasticity (Fjaer et al., 2008). The evaluation of

stresses based on the temperature and pressure build upon the work of Myklestad (1942) and Perkins and Gonzalez (1985).

The induced stresses are added to the virgin in-situ stresses, which may exhibit stress gradients, contrasts in horizontal stresses at the reservoir upper and lower boundaries, and horizontal stress anisotropy. The induced stresses are radially symmetric as are the pressure and temperature fields that cause them, but anisotropy of the initial stress will result in radially anisotropic total stresses.

SRIMA does not consider wellbore stability. The mere presence of the well changes the stress distribution around it (Kirsch, 1898) . However, the main influence of these concentrations is limited to a few borehole radii away from the well. Since we focus on hydraulic fracturing and fault reactivation in the reservoir and seal somewhat away from the well, we discard the stress concentrations at the wellbore. We thus consider the effects far enough from the well to discard stress concentrations at the wellbore, but close enough to discard the radial decrease of induced stresses.

Linear poro-thermo-elasticity can strictly only be employed when failure does not occur. Up to failure conditions, however, the calculations are trustworthy. This is the case for most of the rock mass under study. We have demonstrated that for elastic contrasts between reservoir and bounding layers which are smaller than a factor 4, the approximations developed are acceptable (Section 3.2). Larger contrasts are rare assuming a realistic range of Young's moduli for various rock types.

The coupling between pressure, temperature and stresses is a one-way coupling. As an example, pressures induced by strains that originate from stresses induced by temperature changes are not taken into account. However, the two-way coupling effect are usually only relevant on small scales, close to interfaces between layers or on places where variations in temperature and pressure are large.

2.2.2. *Poro-thermo-elastic equations*

When the temperature and pressure distributions (in terms of their change from initial values, ΔT and ΔP) are known and the mechanical behavior is linearly elastic, the induced stresses and strains ($\Delta\sigma_{ij}$ and ε_{ij},) and the volumetric strain ε_{v} must obey the poro-thermo-elastic constitutive equation. Selecting the sign convention with compressive stresses positive, we have:

$$\Delta\sigma_{\mathrm{ij}} = 2G\left[\varepsilon_{\mathrm{ij}} + \frac{\nu}{1-2\nu}\varepsilon_{\mathrm{v}}\delta_{\mathrm{ij}}\right] + (\alpha_{\mathrm{Biot}}\Delta P + \beta_{\mathrm{T}}\Delta T)\delta_{\mathrm{ij}} \qquad 7$$

Here, G is the shear modulus; ν the Poisson ratio, α_{Biot} is Biot constant, $\beta_{\mathrm{T}} = \alpha_{\mathrm{b}}K = 3\alpha_{\mathrm{T}}K = \frac{\alpha_{\mathrm{T}}E}{1-2\nu}$ the product of the volumetric thermal expansion coefficient α_{b} times the bulk modulus K; α_T the linear thermal expansion coefficient. We further define for later use the thermo-elastic and poro-elastic stress path coefficients

$$\gamma_{\mathrm{T}} = \frac{1-2\nu}{1-\nu}\cdot\beta_T = \frac{E\alpha_{\mathrm{T}}}{1-\nu}$$
$$\gamma_{\mathrm{h}} = \frac{1-2\nu}{1-\nu}\alpha_{\mathrm{Biot}} \qquad 8$$

Eq. 7 needs to be solved with the appropriate boundary conditions; pressure and temperature changes will induce poro-elastic and thermo-elastic strains and stresses.

2.2.3. Thermo-elastic stresses

For a cooled cylinder with a discontinuous temperature profile at the boundary, analytical equations are available for the induced thermo-elastic stresses, both inside and outside the cooled cylinder (Myklestad, 1942; Perkins & Gonzalez, 1985). These can be easily implemented (Candela et al., 2018). We have discretized the temperature profile in the reservoir in 10 steps of equal temperature change and calculate the contribution of each of the resulting cylinders to the stress.

Besides the cooled part of the reservoir, there is also cooling of part of the seal and the base. For the effect of this zone, we employ an induced horizontal stress in the cylinder of $\gamma_{\mathrm{T}}\Delta T$. Outside it is approximately zero. Vertical induced stresses are zero both inside and outside such cylinders. These equations follow from the Myklestad solutions for a very flat cooled cylinder, i.e. a cylinder with a large radius / height ratio, and at radial locations well within the cooling radius.

Myklestad developed his equations for a cooled or heated cylinder in a full space with homogeneous elastic properties. Realistic geological scenarios require the possibility of incorporating inhomogeneities. For the thermo-elastic stresses these would be properties which are different for different layers. We applied the analytical correlations developed for homogeneous subsurface to situations with an elasticity contrast between reservoir and seal and base, but with dedicated γ_{T}: for thermoelastic stresses in the reservoir we take the reservoir value; for thermo-elastic stresses in the seal and base we take the seal and base values when calculating the horizontal components and the value for the reservoir for the vertical components. This was based on a benchmark exercise. Results of the validation are given in Section 3.2.

Our estimate for the thermal stress is therefore Myklestad's solution both inside and outside the cooled cylinder in the reservoir, supplemented with a term proportional to the temperature change at positions outside that region.

2.2.4. Poro-elastic stresses

Poro-elasticity and thermo-elasticity are, mathematically speaking, analogous (Geertsma, 1957; Wang & Dusseault, 2003). However, the input distribution of temperature and pressure in our system is very different, therefore a different treatment is required. Notably, the pore pressure in the reservoir is a logarithm function of the distance from the well. An obvious approach would therefore be to discretize the pressurized area and numerically integrate the contribution of pressurized "ring elements" to the poro-elastic stress (Geertsma, 1973). Such approach is beyond the scope of our current setup. We have chosen to approximate the effect of the complete pressurized reservoir with the effect of a single pressurized cylinder. The pressure and the radius of this cylinder depend on the position where we want to evaluate the stresses. Clearly, a calibration is crucial in this approach.

The best approximation that we found, in terms of simplicity and accuracy, uses an equivalent pressurized cylinder, r_{eq}, defined as radius $r_{\mathrm{eq}} = 10r$ and an equivalent pressure, ΔP_{eq}, given by $\Delta P_{\mathrm{eq}} = \Delta P\left(\frac{1}{10}r_{\mathrm{eq}}, 0\right)$ for the poro-elastic effect at a position $(r, z); |z| \leq \frac{h}{2}$ in the reservoir. In the seal and underburden r_{eq} becomes $r_{\mathrm{eq}} = 10r + \left(|z| - \frac{h}{2}\right)$ and the equivalent pressure is given by $\Delta P_{\mathrm{eq}} = \Delta P\left(\frac{1}{10}r_{\mathrm{eq}}, 0\right)$ for the poro-elastic effect at a position $(r, z); |z| > \frac{h}{2}$. Figure 2 visualizes the concept for the equivalent pressurized cylinder. The factor $\gamma_{\mathrm{T}}\Delta T$ that is present in the thermo-elastic expressions is replaced by $\gamma_{\mathrm{h}}\Delta P_{\mathrm{eq}}$.

The effect of the pressurization of parts of the seal and the underburden is treated completely analogous to the thermo-elastic effect of the cooling of those parts: we add a term $\gamma_h \Delta P$ to the cylinder contribution in the seal and the underburden, with the actual pressure at the point of calculation.

Introducing elasticity contrasts at the interfaces had only minor effect on the resulting poro-elastic stresses. This is due to the form of stress path coefficients. The elastic modulus is directly present in the coefficient for thermo-elasticity; it is absent in the coefficient for poro-elasticity. Only some effect of the Poisson ratio remains.

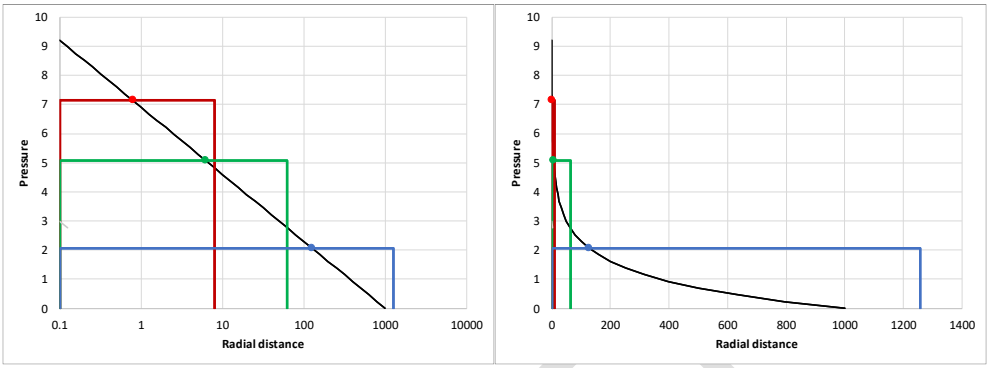

Figure 2 Concept of equivalent pressurized cylinder. The poro-elastic fields at the position of the red, green, and blue dots originates from the pressure in the reservoir that is given by the black curve. It is approximated by Myklestad's correlations for a pressurized cylinder with constant pressure inside it and a radius of 10 times the point of interest: the red, green and blue curves. Left and right show the same curve but with linear and logarithmic distribution of the radial distance

2.2.5. *Total stresses*

The calculated thermo-elastic and poro-elastic contributions to the stress are radially symmetric. If the virgin horizontal stresses are anisotropic, the rotational symmetry of the end product is broken and the thermo-elastic and poro-elastic contributions must first be transformed to the cartesian coordinate system:

$$\sigma_{cart}^{TPE} = \begin{pmatrix} \sigma_{xx}^{TPE} & \sigma_{xy}^{TPE} & \sigma_{xz}^{TPE} \\ \sigma_{xy}^{TPE} & \sigma_{yy}^{TPE} & \sigma_{yz}^{TPE} \\ \sigma_{xz}^{TPE} & \sigma_{yz}^{TPE} & \sigma_{zz}^{TPE} \end{pmatrix}$$
$$= \begin{pmatrix} \cos\varphi & \sin\varphi & 0 \\ -\sin\varphi & \cos\varphi & 0 \\ 0 & 0 & 1 \end{pmatrix} \begin{pmatrix} \sigma_r^{TPE} & 0 & \sigma_{rz}^{TPE} \\ 0 & \sigma_\theta^{TPE} & 0 \\ \sigma_{rz}^{TPE} & 0 & \sigma_z^{TPE} \end{pmatrix} \begin{pmatrix} \cos\varphi & -\sin\varphi & 0 \\ \sin\varphi & \cos\varphi & 0 \\ 0 & 0 & 1 \end{pmatrix} \quad (9)$$
$$\varphi = \operatorname{atan}\left(\frac{y}{x}\right)$$

This expression makes use of the fact that induced shear stresses along the tangential coordinate must be zero because of the symmetry. The thermo-poro-elastic contributions to the stress are added to the virgin stresses. The virgin stress in cartesian coordinates is obtained through a rotation of the stress in principal value orientation, $\begin{pmatrix} \sigma_{h0} & 0 & 0 \\ 0 & \sigma_{H0} & 0 \\ 0 & 0 & \sigma_{v0} \end{pmatrix}$, over the angle of the direction of the maximum horizontal stress with regard to the north.

2.3. Fracture estimation

We have implemented a conservative estimate of how far a hydraulic fracture could grow. The stresses are determined by the temperature field and the pore pressure. Once a fracture starts developing, however, the pressure in the fracture is not the pore pressure at that location anymore, but it is controlled by the pressure in the injection point. We thus estimate the pressure that would be present in a fracture if it would exist and if there would not be pressure losses due to frictional flow. This pressure, P_{hf}, at depth z, is the calculated pore pressure of fluid entering the injection layer at the wellbore, corrected only for the hydrostatic head originating from the fluid density and the depth difference between injection point and point of calculation:

$$P_{hf} = P_{wb} + (z_{wb} - z)\rho_w g \qquad 10$$

Here, P_{wb} is the fluid pressure when entering the reservoir at the wellbore at depth z_{wb}, ρ_w is the fluid density and g the gravitational acceleration constant.

The potential vertical extent of a hydraulic fracture is then calculated as the maximum extent at which this pressure is larger than the minimum in-situ stress plus the fracture overpressure, that is the minimum and maximum depths at which $P_{hf} > \sigma_3 + \Delta P_{hf}$, in which σ_3 is the minimum in-situ stress and ΔP_{hf} the fracture overpressure. Figure 3 demonstrates the concept. How results for tensile failure are handled in stochastic simulations is addressed in Section 2.5.

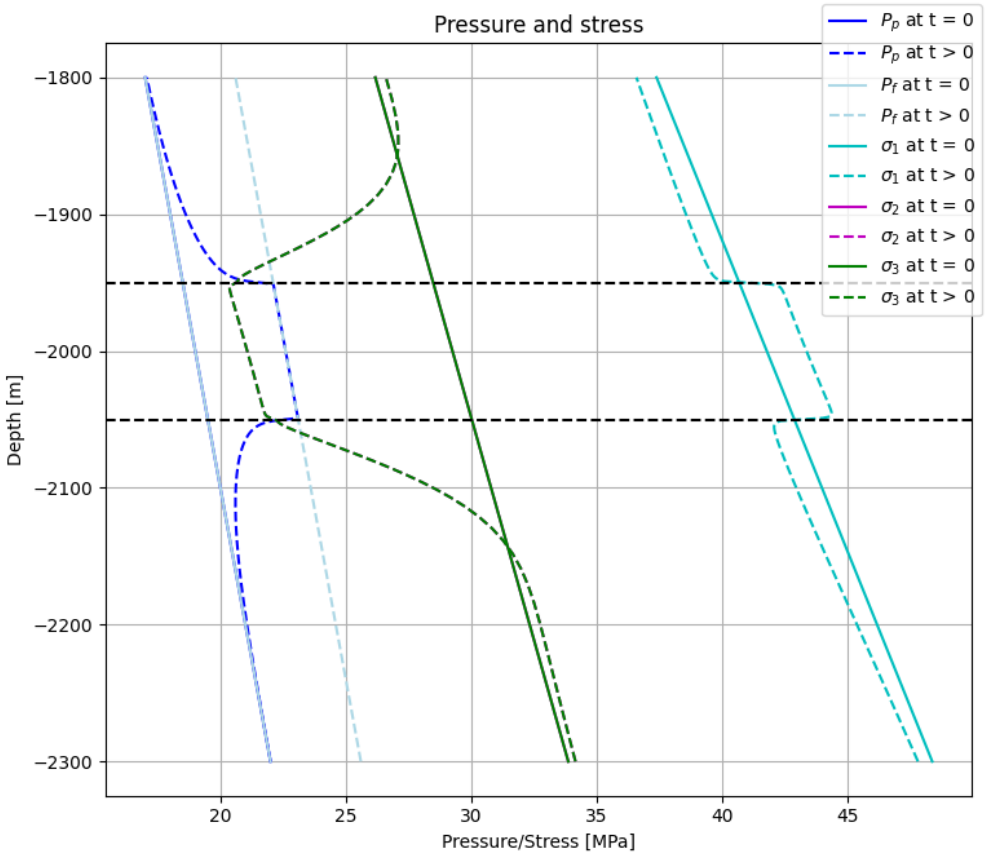

Figure 3 Demonstration of Hydraulic Fracture Potential (with $\Delta P_{hf} = 0$). Significant cooling has decreased the horizontal stresses; pressurization has increased the vertical stress in the reservoir. While the modelled pore pressure decreases rapidly outside the injection

layer, the pressure in a potential fracture will be high because of direct hydraulic connection with the wellbore pressure. Hydraulic fractures can develop where the "fracture pressure", P_f, is larger than the minimum in-situ stress σ_3

2.4. Shear Failure estimation

A virtual fault is included in the model geometry with a given dip θ and dip direction φ (Figure 5). The dip direction is defined with regard to the northern direction. The stresses are defined with respect to the same coordinate system; the initial stresses are dependent on the direction of the maximum horizontal stress σ_H (in case $\sigma_h \neq \sigma_H$). The shear stress and the normal stress on the fault are computed from the traction of the full stress tensor on the fault plane.

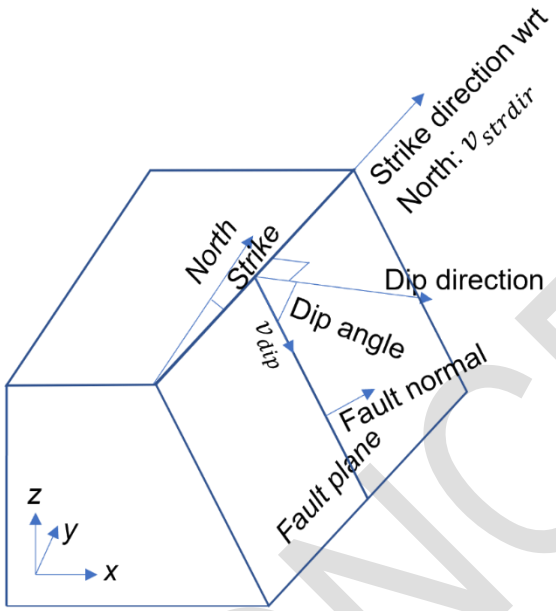

Figure 4 Definition of fault plane. The dip direction is perpendicular to the strike.

The fault normal is defined as

$$\mathbf{n}_{fault} = \begin{pmatrix} \sin\varphi \ \sin\theta \\ \cos\varphi \sin\theta \\ \cos\theta \end{pmatrix} \quad 11$$

Then the traction on the fault, and the normal and shear components of it are given by

$$\mathbf{T} = \sigma \cdot \mathbf{n}_{fault}$$

$$\sigma_n = \mathbf{T} \cdot \mathbf{n}_{fault} \quad 12$$

$$\tau = \sqrt{\mathbf{T} \cdot \mathbf{T} - \sigma_n \cdot \sigma_n}$$

The Mohr Coulomb failure criterion is assumed for the fault strength

$$\tau_f = \mu(\sigma_n - P) + C \quad 13$$

where τ_f is the shear stress at which shear failure occurs, μ is the static friction coefficient, P is the pressure at the fault and C the cohesion. The proximity to failure can be expressed as the Shear Capacity Utilization (SCU)

$$SCU = \frac{\tau}{\tau_f} = \frac{\tau}{\mu(\sigma_n - p) + C} \qquad 14$$

An SCU of 0 indicates the lack of any fault shear stress (stable), and an SCU of 1 indicates the Mohr-Coulomb criterion has been reached and fault slip can occur. Note that fault slip and stress redistribution is not modeled in SRIMA. Therefore, the state of stress can be such that the SCU on the virtual fault is larger than 1.

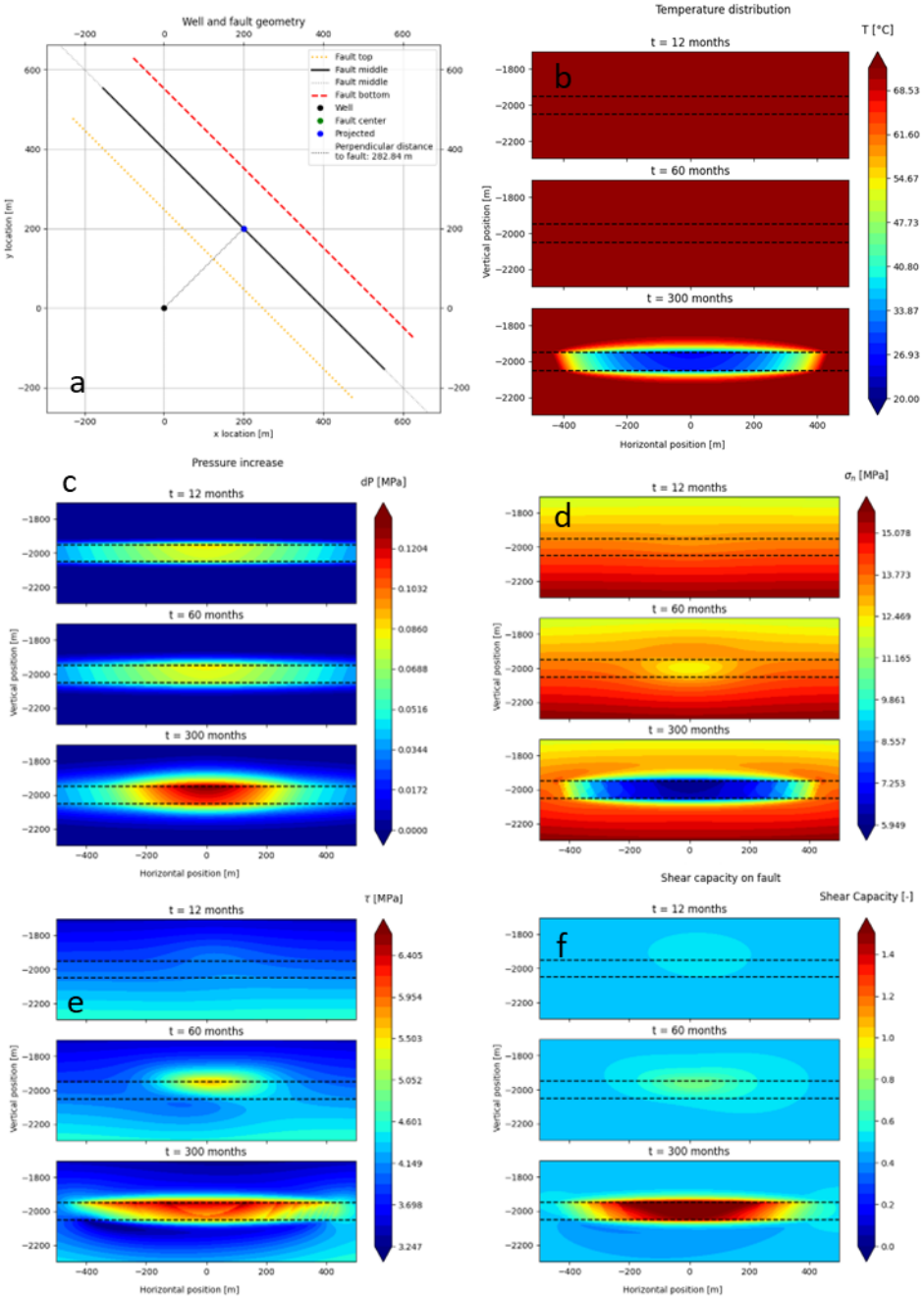

Figure 5 Example temperature, pressure, and stress changes on a fault nearby the injection well, as computed in SRIMA. Reservoir depth is indicated by the dashed lines (b-f). A) position of injection well and fault, top view, b) temperature changes on fault, c)

pressure changes on fault, d) normal stress changes on fault, e) shear stress changes on fault, f) shear capacity utilization (SCU) on fault, at three different points in time.

An example of fault stresses computed in a typical model realization in SRIMA is shown in Figure 5. As the cold front (front of the cooled volume) reaches the fault, the normal stress decreases and the shear stress increases. The net effect is an increase in SCU. Note that even before the cold front reaches the fault, small stress changes occur due to elastic stress transfer. The stress signature is dominated by the temperature changes; mostly pressure changes near the injection well are limited and decay logarithmically with distance from the injection well (equation 4). The cooled and stressed fault area is wider near the top of the reservoir. This is due to the fault dipping away from the injection well.

When a fault orientation is not known, the slip tendency can be calculated for the fault orientation that is most prone to failure. The calculation does not require stresses for all possible orientations; it suffices to determine the maximum and minimum effective principal stresses σ_1' and σ_3', and the associated shear capacity of the rock, which is a measure for the proximity of the Mohr circle to the failure envelope. The shear capacity utilization for the critical orientation is calculated as

$$SCU = \frac{\sqrt{1+\mu^2}(\sigma_1' - \sigma_3')}{\mu(\sigma_1' + \sigma_3') + 2C} \qquad 15$$

Failure will occur if the value for the shear capacity is larger than unity. The measure is defined locally. How results for shear failure are handled in stochastic simulations is addressed in Section 2.5,

2.5. Stochastic Model

An important aim of SRIMA is to assess probabilities of failure. Therefore, the implementation has been embedded in a stochastic framework. First, the parameters which are uncertain are identified. Then, many realizations of sensible model parameter sets are created. The parameters are drawn from a bi-triangular probability distribution with an expected value and maximum and minimum values. This way, the expected value has the largest probability.
All realizations are employed in a semi-analytic calculation. The results in terms of pressures, fault activation, hydraulic fractures, are calculated for every realization. The ensemble of realizations thus produces ensembles of values for pressures and failure measures, which can then be used to make probabilistic estimates. Correlations between estimated measures for failure and uncertain input parameters can also be used to steer information gathering. Priority can then be given to information gathering of parameters that have the largest impact on the calculated failure probability.
One assessment of the stochastic results is in the form of so-called cumulative density plots. Consider, as an example, a stochastic run with an ensemble of 2500 calculations performed along a vertical line at the position of the wellbore. We performed calculations after 1, 5, and 25 years of injection. For every output variable we then also have an ensemble of 2500 outcomes for these three times. Figure 6 shows the cumulative occurrence of hydraulic fracture potential and for shear failure extent smaller than the value on the horizontal axis. We see that for the three times chosen, the probability for potential hydraulic fracture in the seal increases from 0.47 to 0.56. The probability of shear fractures is larger, which is understood through the

mechanism of shear failure occurring for stresses which are still compressive. Some realizations result in shear failure of the complete 100-m thick seal, even some already early in time, due to critical stressing of the virgin reservoir. The probability of developing larger fractures increases with time. P90, P50 and P10 values can be determined by simple intersection of these curves with the 0.9, 0.5 and 0.1 cumulative probability, Figure 6. The points indicate the probability of 0.9, 0.5, and 0.1 of finding a length larger than the indicated length.

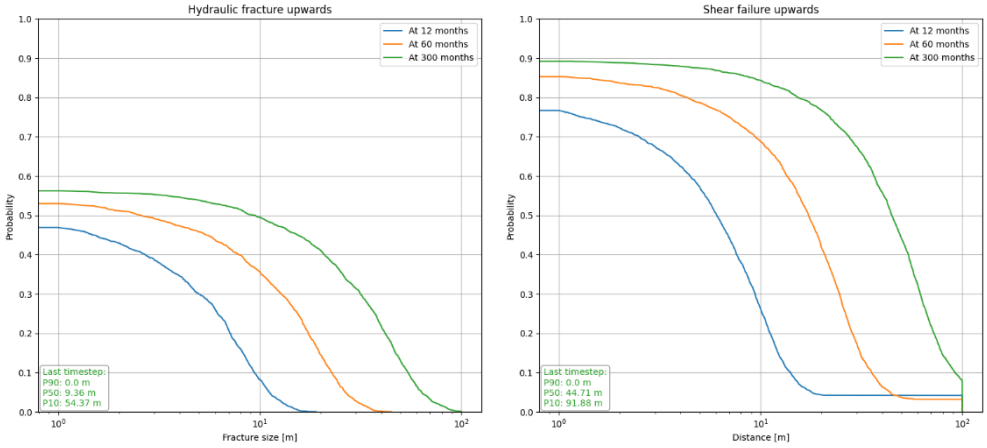

Figure 6 Cumulative density plots for the probability of potential hydraulic fractures larger than a certain size (left) and for the extent of shear failure (right)

Operators also need guidance with respect to allowed injection pressures. A possible question could be “What is the maximum value of the pressure for which the probability of not creating a hydraulic fracture larger than, e.g., 50% of the seal thickness (i.e. the probability that injection is safe) is at least, e.g. 90%.” To answer such questions, the stochastic output values for hydraulic fracture height and pressure need to be correlated. The pressure values are grouped in intervals (“bins”) with a certain number of realizations, and for each bin the number of fractures staying with the predetermined limit is determined. The average pressure within each bin and the proportion of safe realization are then plotted and related with a suitable model. This allows to determine an estimate of the safe value of the pressure.

How results for tensile failure and for shear failure are combined in the stochastic mode of calculations is best demonstrated with an example. Consider the same ensemble as above. Each of those calculations has an outcome in pressure profile, total stresses, and based on that also creation and extent of hydraulic fracture and shear fracture in seal and base. We can visualize the parameters relevant for the question at stake by plotting the potential vertical extent of a hydraulic fracture against the wellbore pressure of the same realization. The result is a scatter plot, of which an example is given in Figure 7 (top). Every realization corresponds with a point in the Pressure – Fracture potential plot. Clearly, realizations with large fractures into the seal tend to have a larger wellbore pressure. However, this is only a statistical correlation, since other input parameters also have their influence. Important other parameters are, for instance, the virgin minimum principal stress and the injection temperature.

To support governance guidance, a further stochastic analysis is needed. Our approach is to divide the range of possible pressure outcomes in intervals and determine for each of these intervals the probability of exceeding the allowed fracture growth potential. We have chosen to have intervals with approximately the

same number of realizations, and approximately the same number of realizations per interval as numbers of intervals themselves. For the ensemble size of 2500 realizations we thus have 50 pressure intervals with each 50 realizations. For each of these intervals, we determine the share of “unsafe” realizations, and we visualize them. The procedure is performed for the bottomhole pressure as well as for a pseudo wellhead pressure, since the wellhead pressure is the number with which operators deal. The wellhead pressure equals the bottomhole injection pressure, corrected for the hydrostatic head in the fluid column and the frictional pressure drop – however, since determination of the frictional pressure drop requires a dedicated well flow model, we have left this one out of the calculation and stick to the conservative estimate which is what we call the pseudo wellhead pressure: the bottomhole injection pressure minus the hydrostatic head of the water column to the surface. The outcome for the two calculations is represented as the dots in Figure 7 (middle) and Figure 7 (bottom). Figure 7 (bottom) shows some pseudo well head pressures which are negative. This is related to the possibility of underpressure (pressure lower than hydrostatic) in the reservoir at the start of the simulation. Finally, a value is sought for the maximum value of a safe pressure. In the example we define the safe pressure as the pressure for which the probability of not creating a hydraulic fracture larger than 50% of the seal thickness is at least 90%. This requires a fit of the scatter points in the two plots to a theoretical relationship. In the absence of further theoretical observations and considering the many uncertain parameters present, a Gaussian distribution is the best choice for this relationship. The cumulative density function of such a distribution has only two free parameters: the center of the distribution, μ, and its width, σ. The Gaussian distribution then is

$$g(x) = \frac{1}{\sigma\sqrt{2\pi}} \exp\left(-\frac{(x-\mu)^2}{2\sigma^2}\right) \quad 16$$

The cumulative distribution function as we describe it (essentially 1-*cdf*) is

$$1 - cdf = \frac{1}{2}\left[1 - \mathrm{erf}\left(\frac{x-\mu}{\sigma\sqrt{2}}\right)\right] \quad 17$$

The parameters μ and σ are determined by minimizing the mismatch between the scatter points in Figure 7 (middle and bottom) and the value from Eq. 16. The 90% value for a safe pressure, finally, is determined by the value at which Eq. 16 with the fitted parameters equals 0.9.

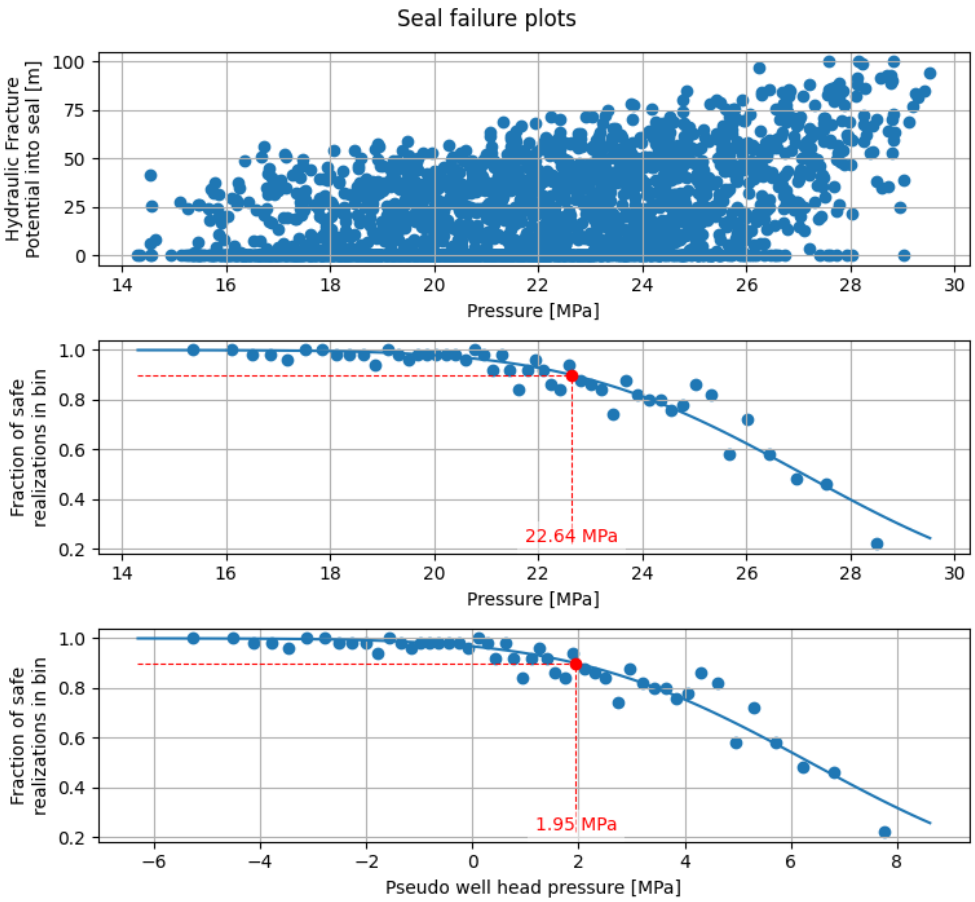

Figure 7 Correlation of hydraulic fracture potential with pressure

2.6. Choices for operational parameters

The driving force behind the stress changes and the associated modeled failure is the injection of a fluid of constant temperature at a constant rate. Changing temperatures and rates would preclude the use of analytic expressions, due to the complex interplay between advection in the injection layer and diffusion in the bounding layers. A full realistic injection scheme can therefore not be modelled. For the injection rate, we address this by calculating an increased pressure drop for the maximum rate, as compared to the average rate. The average injection rate will determine the position of the temperature regions and the associated injection fluid viscosity, while the injection rate will determine the pressure gradient and the associated pressure drop. Because the calculation of pressure is with semi-steady-state conditions, this is warranted. For the temperature, the approximation gives the first order effect; stochastic calculations can be deployed to map the effect of the temperature range. The thermo-elastic stresses will thus be based on the best estimate of the distribution of the temperature, while the poro-elastic stresses will be based on the maximum injection rate.

2.7. Deterministic seismic hazard analysis

According to Dutch Mining regulations (MBR) each production license application should contain an analysis of scenario-based ground motions (see Mijnlieff et al., 2023). This includes a seismic hazard analysis which expresses seismic hazard in

terms of expected ground motions such as peak ground acceleration, PGA, or peak ground velocity, PGV. For the Seismic Hazard and Risk Assessment for geothermal operations ("*SDRA Geothermie*" in Dutch) the largest credible earthquake (LCE) and the resulting PGV is considered, which is an important ground motion parameter for Damage State 1. The details of the seismic hazard analysis are provided in the following sections.

To obtain the PGV values a seismic hazard analysis must be performed, which can be of a deterministic or probabilistic nature (Table 1). Probabilistic seismic hazard analysis (PSHA) is often used as the standard method for computation of seismic hazard; e.g., the PSHA for the Groningen field (Bourne & Oates, 2017; Dost, Ruigrok, & Spetzler, 2017; TNO, 2020). In such an analysis the ground motion with a specified annual probability of exceedance is computed, taking into account specific sources and relevant uncertainties in terms of location, size, seismicity rates, etc. Deterministic hazard analysis (DSHA) is nowadays less commonly used, but is still used for specific constructions (dikes, nuclear facilities, hospitals, etc.) in areas where the seismicity is low or monitoring data of the earthquake distribution is absent. In case of a deterministic seismic hazard assessment the largest credible earthquake magnitude (M_{LCE}) is assumed on one or more sources (i.e., nearby faults), without knowing its annual probability of occurrence. This magnitude is based on expert judgement of available information regarding the earthquake source. The M_{LCE} is then used to compute ground motions through ground motion prediction equations (GMPEs). A certain measure of these ground motions is then used to express seismic hazard, though this is not specified per time interval as obtained for PSHA. For the current SDRA Geothermie we adopt a (pseudo) deterministic hazard analysis workflow (DSHA), as (observational) data required to inform a probabilistic hazard analysis at the location of geothermal sites in the Netherlands is lacking. Uncertainty in PGV resulting from the GMPE uncertainties is accounted for.

Table 1 Basic ingredients of Deterministic Seismic Hazard Analysis (DHSA) and Probabilistic Seismic Hazard Analysis (PSHA), as well as the implementation for the SDRA Geothermie (shaded cells).

	DSHA basic steps	PSHA basic steps
Sources	Mapped fault(s) nearby site of interest.	Identification of all possible sources, including uncertainty in location, fault length, etc.
	Here: One fault, the fault intersected by the cold front. The earthquake source is assumed to lie at the point on the fault closest to the injection well.	
Seismicity rate	Not considered	Frequency-magnitude distribution or Gutenberg-Richter (GR) relationship to describe earthquake rates of all magnitudes, at all sources, including uncertainty in the distribution.

Maximum Magnitudes	Largest Credible Earthquake (LCE)	Probability distribution of maximum magnitudes M_{max} of the different sources, in combination with a truncation model to the Gutenberg Richter. M_{max} can also be based on expert judgement, but is typically included as a frequency-magnitude distribution instead of a single value.
	Here: LCE based on fault area affected by the induced stresses, as computed in SRIMA. This is not a single LCE, but a distribution of LCEs following from the stochastic analysis in SRIMA (section 2.5)	
Ground motion	From empirical Ground Motion Predication Equation (including uncertainty).	Empirical Ground Motion Predication Equations including full definition of uncertainty are used to compute the probability distribution of ground motion for each of the sources.
	Here: BMR2 (Ruigrok & Dost, 2020) GMPE model, including the uncertainty, is used to compute the PGV values for each MCE.	
Hazard	Typically one or more ground motion parameters are used to characterize seismic hazard.	All uncertainties are combined to yield the probability that a certain ground motion parameter (PGA or PGV) can be exceeded at a certain site within a certain time.
	Here: PGV distributions for each MCE combined to compute probability of exceedance. The P10, P50 and P90 values (at the epicenter) are used to characterize seismic hazard. In addition, the probability of exceedance curve is given for 2 mm/s, also for P10, P50, and P90.	

2.7.1. Event location

The stressed fault area will be used as a proxy for the largest credible earthquake magnitude, M_{LCE} (next section). The centre of the stress fault area lies (approximately) at the mid-depth of the reservoir, at the fault location closest to the injection well (Figure 8). No uncertainty in fault location is accounted for in the DSHA, and the location remains the same for all model realizations.

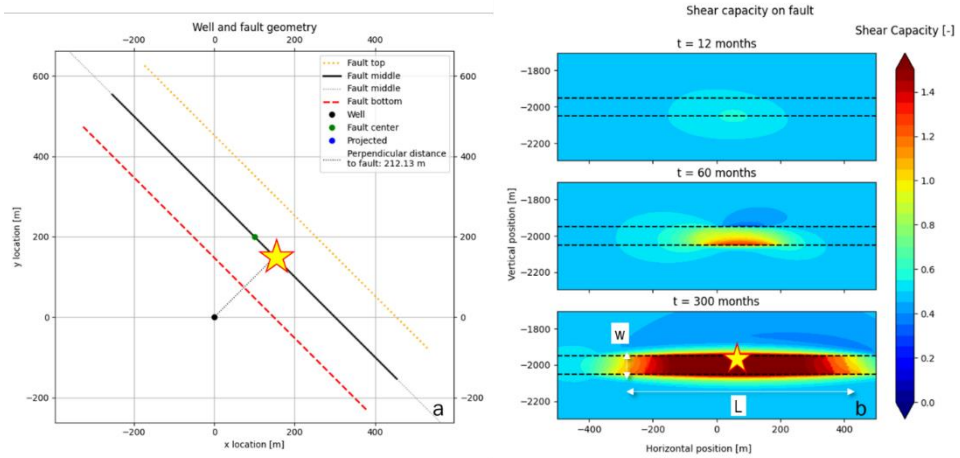

Figure 8 Illustration of the source location. a) Top view of the injection well and fault. b) On-fault view of the shear capacity utilization (SCU) indicative of the slip zone (SCU≥1). Hypocenter location is indicated with the star.

2.7.2. *Largest Credible Earthquake (LCE) magnitude*

The results from SRIMA are used to estimate the largest credible earthquake magnitude M_{LCE}, which is used in the DSHA. Modeling of fault slip, dynamic rupture and/or modeling of seismicity rates are beyond the scope of a simplified and easy-to-use tool like SRIMA, and moreover, monitoring data to validate such computations are not available. Hence, magnitudes of seismic events are not explicitly modeled. Instead, the fault area affected by the geothermal operations is used as a proxy for the fault area linked to the largest credible earthquake magnitude. This estimate is comparable to the estimates of M_{max} for the small gas fields (SodM, 2016).

The area *A* of the part of the fault over which slip occurs (slip zone) is an important ingredient determining the seismic moment, which is indicative for the size of an earthquake (Aki, 1966):

$$M_0 = GAd \quad (18)$$

The seismic moment furthermore depends on the shear modulus of the surrounding rock *G* and the average fault slip *d* within the slip zone. Through elastic dislocation theory, the slip within slip zone can be related to the static stress drop $\Delta\tau$ – i.e. the difference between the shear stress before and after the slip event averaged over the slip zone. Using this relation, the seismic moment equation can be rewritten to (Kanamori & Anderson, 1975)

$$M_0 = \left(\frac{\tilde{L}}{C}\right) A\Delta\tau \quad (19)$$

Where C is a proportionality factor close to 1, depending on the fault geometry, and $\tilde{L}$ is the characteristic fault dimension which also depends on the geometry (e.g. $\tilde{L}$ is the radius for a circular fault slip zone, and width *w* for dip-slip fault slip zones). For buried dip-slip faults (normal faults) as representative for faulting in the Netherlands, the corresponding seismic moment M_0 [Nm] is given as (Kanamori & Anderson, 1975; Starr, 1928)

$$M_0 = \frac{3\pi}{8}\Delta\tau w^2 L \quad (20)$$

Where L is the along-strike dimension of the slip zone and w is the along-dip dimension of the slip zone; i.e. for a vertical fault the w would be the depth interval of the slipping zone. Note the square dependency on the slip zone width. The seismic moment can be converted to a moment magnitude M_w through (Hanks & Kanamori, 1979)

$$M_w = \frac{2}{3}\left(\log_{10}(M_0) - 9.1\right) \quad (21)$$

The moment magnitude M_w has an approximate 1:1 scaling with the empirical local magnitude M_L or Richter magnitude, which was traditionally used to denote earthquake size. However, (small) differences may exist between the two scales depending on earthquake magnitude, with e.g. a M_w being 0.2 smaller than M_L for Groningen earthquakes with magnitudes 2.5 – 4 (Dost, Edwards, & Bommer, 2016).

We base our estimates of the along-dip and along-strike dimensions of the slip zone on the fault area affected by the geothermal operations, comparable to what is done for the small gas fields. Whereas for the small gas fields the intersection of the largest fault with the gas-filled parts of the reservoir is taken as the affected fault area, here the affected fault area is determined using a stress criterion. To distinguish the magnitude computed here from maximum magnitudes as typically determined from e.g. the truncation of the Gutenberg-Richter frequency-magnitude relationship or the upper bound to recurrence curves, we name the magnitude of the largest credible earthquake M_{LCE}.

M_{LCE} is computed from the calculated fault stresses as follows. For each iteration, for a given timestep, the computed SCU distribution (Equation 14) on the fault plane is considered.

- The slip zone is then defined as the fault area where SCU ≥ 1.
- The slip zone width w is defined as the average of the along-dip fault length within the slip zone where SCU ≥ 1.
- The slip zone length L is defined as the average of the along-strike length within the slip zone where SCU ≥ 1.

Furthermore a constant stress drop over the slip zone is assumed, which can be set by the user, typically in the range between 1-5 MPa. Stress drops computed for events within the Groningen field mostly fall below 2 MPa; note however that substantial uncertainty exists in these values as the derived stress drop is dependent on the model assumed for the inversion. Using Equations 20 and 21 the resulting magnitude can be computed.

For the example shown in Figure 9, the average along-dip fault length w is 104 m, and the average along-strike fault length is 244 m. For a stress drop of 5 MPa (the value used for the small gas fields) the resulting seismic moment is $1.6 \cdot 10^{13}$ Nm and the corresponding M_w is 2.7.

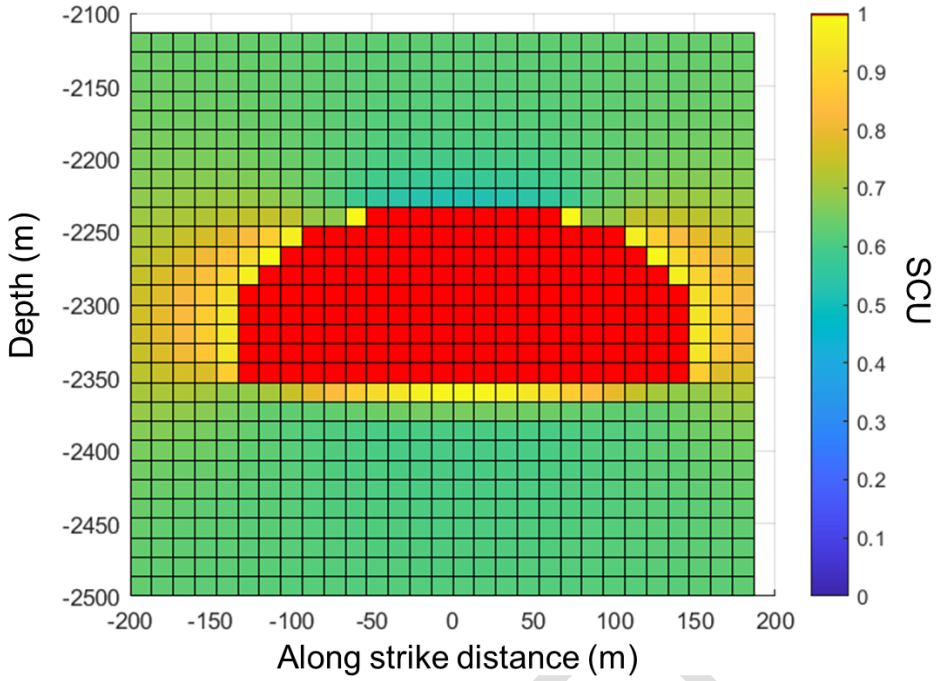

Figure 9 Example of determining the area from SRIMA. In the plot computed SCU values on the fault plane are shown, with red SCU ≥ 1.

Various assumptions underlie this approach:

- (conservative) it is assumed that all the fault slip within the slip zone is *seismic* slip. However, part of the deformation on the fault may be accommodated as aseismic slip. When more data becomes available in the future, it is recommended to better constrain the aseismic/seismic partitioning of induced fault slip.
- (not conservative) fault slip and resulting stress transfer is not modeled in SRIMA. Taking into account fault slip and stress redistribution would lead to a larger fault area where SCU equals 1. For the logarithmic dependence of magnitude on moment and area the effect on magnitude is likely small. In future models, the effect of fault slip on the perturbed zone could be accounted for, or an SCU threshold of e.g. 0.9 could be assumed to account for this effect.
- (not conservative) it is assumed slip cannot propagate far beyond the stressed fault area. Such an assumption is deemed valid for a low-stress environment, which is typically assumed for the upper kms of the Dutch subsurface (Bakx, Buijze, & Wassing, 2022).
- (conservative) another assumption is that the stress build-up on the fault is released in a single event. This is regarded conservative; given the gradual buildup of stress on the fault, progressive fault reactivation through multiple smaller events is more likely.
- furthermore it is assumed that the slip zone can be confined to a finite size fault. If a fault terminates within the cooled and stressed rock volume around the injection well, the fault terminus is considered the end-point for the along-strike slip zone length.

The stress drop has a big impact on the computed magnitude (Equation 20). For the M_{max} calculation of the small gas fields, a fixed stress drop of 5 MPa is considered (SodM, 2016). This value was based on stress drops of natural events. Also, stress drop analysis for Groningen induced events yielded values mostly between 0.1 and 2 MPa (note there may be a factor 5 uncertainty in these values). However, whereas depletion and the reduction of pore pressure leads to a more compressive state of stress, for geothermal sites cooling may lead to a less compressive state (see e.g. Buijze et al., in press). It may therefore be reasonable to assume a lower stress drop for the magnitude calculation of geothermal sites. When more (micro)seismic observations become available in the future, it is recommended to build a stress drop database with which the SDRA can be informed.

2.7.3. Peak ground velocity: BMR2 GMPE

After computing the largest credible earthquake magnitude for different timesteps in each model iteration, the distribution of corresponding peak ground velocities (PGV) is computed. To translate magnitude to ground motion, ground motion prediction equations (GMPE) are required. Here we use the BMR2 GMPE model that has been developed for small earthquakes outside of the Groningen field (Ruigrok & Dost, 2020). This model has been derived on the basis of recorded PGV values resulting from M 1.5 – 3.5 induced earthquakes in the Netherlands occurring outside of the Groningen field. The PGV values are taken from the horizontal recordings of a seismic station. There are three definitions for the PGV:

- PGV_{geo}: the geometric mean of the absolute values of the two horizontal components.
- PGV_{max} : the maximum absolute value of the two horizontal components.
- PGV_{rot}: the combination of the two components to compute the maximum value in the horizontal plane.

$PGV_{geo} < PGV_{max} < PGV_{rot}$, and in the SDRA we will use the PGV_{rot} value as it is the most conservative value. From now on we use PGV as relating to PGV_{rot}.

The BMR2 model is a modification of the Bommer model, which was developed specifically for the Groningen field (Bommer et al., 2019). The Bommer model yielded the best fit with the PGV database for values outside Groningen, compared to three other GMPE models (Ruigrok & Dost, 2020). Only in the first few kms from the source the Bommer model tended to overestimate the ground motions. To reduce the misfit, the Bommer model was adapted to include the hypocentral depth in the computation of the source-site distance term; the adapted model is called the BMR2 model.

The Bommer and BMR2 (Ruigrok & Dost, 2020) models are parameterized as

$$\ln(PGV) = c_1 + c_2 M + g(R^*) \quad (22)$$

Where M is the magnitude, $g(R^*)$ is a geometrical spreading term, which is a function of the point-source distance R^*, which for the BMR2 model is

$$R^* = \sqrt{R^2 + D^2 (e^{\epsilon_1 M - \epsilon_1})^2} \quad (23)$$

with epicentral distance R and event depth D. The geometrical spreading term is split over 3 distance ranges:

$$g(R^*) = c_4 \ln(R^*) \qquad R^* \leq d_1 \quad (24)$$

$$g(R^*) = c_4 \ln(d_1) + c_{4a} \ln(R^*/d_1) \quad d_1 < R^* \leq d_2 \qquad 25$$

$$g(R^*) = c_4 \ln(d_1) + c_{4a} \ln(d_2/d_1) + c_{4b} \ln(R^*/d_2) \quad R^* > d_2 \qquad 26$$

The coefficients for the PGV_{rot} are summarized in Table 2. The uncertainty in these PGV values is given by an intra-event standard deviation ϕ of 0.53613, an inter-event standard deviation τ of 0.25242, and a total standard deviation σ of 0.59268 (all given in ln(PGV)).

Table 2 Coefficients for PGV_{rot} for the BMR2 GMPE model.

Coefficient	Value	Unit	Coefficient	Value	Unit
c_1	2.2800	-	ϵ_1	0.0600	-
c_2	2.2835	-	ϵ_2	1.1300	-
c_4	-4.2800	-	d_1	8.10	km
c_{4a}	-0.8000	-	d_2	11.62	km
c_{4b}	-1.7000	-			

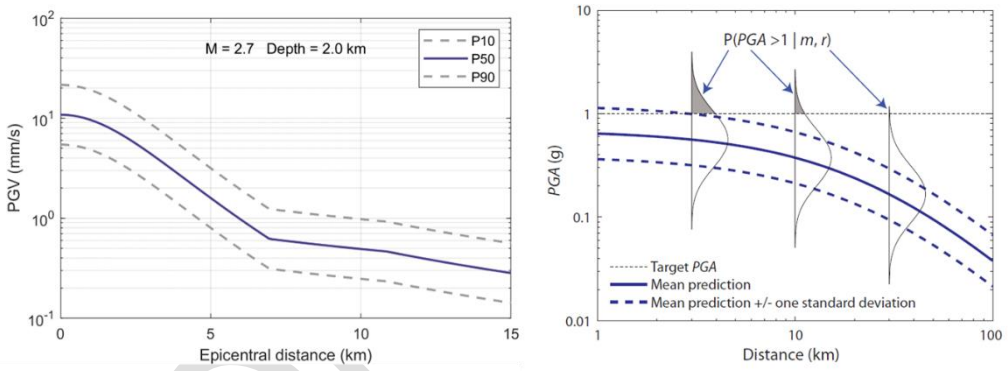

Figure 10 a) Example of PGV values with epicentral distance, for the BMR2 models and a M_L 2.7 event at 2.0 km depth. b) Example of pdfs of PGA at several distances, which is important to account for when deriving probability of exceedance values (From: Baker et al., 2021).

2.7.4. Peak ground velocity: implementation in SDRA Geothermie

For each model iteration, the largest credible earthquake magnitude value is computed. This value is used to compute the PGV distribution at various epicentral distances. To compute PGVs it is assumed that the moment magnitude is equal to the local magnitude, which is the magnitude format on which the BMR2 GMPEs were based.

It is important to take into account the full probability distribution of all model realizations when considering probability of exceedance values (Figure 10). All computed probability density functions (pdfs) have the same binning and each realization, transformed to PGV distribution, is assumed to be equally likely. These pdfs are added and normalized to yield the total probability density function of all model realizations (Figure 11a), at each epicentral distance. The pdf is converted to

a probability of exceedance curve (Figure 11b). From this curve, various percentiles can be obtained, e.g. the P50 value as shown in Figure 11b. In addition, the probability of exceeding a certain threshold value (e.g. 2 mm/s) can be obtained (here ~0.72). Note that also the realizations are taken into account which did not lead to fault reactivation – i.e. did not generate a magnitude at all. These do not contribute to the pdfs and exceedance curve, but as we normalize by the number of realizations the no-seismicity cases are reflected by the exceedance curve not attaining 1 at the lower end. In the example below, 1 out of 15 realizations did not lead to seismicity.

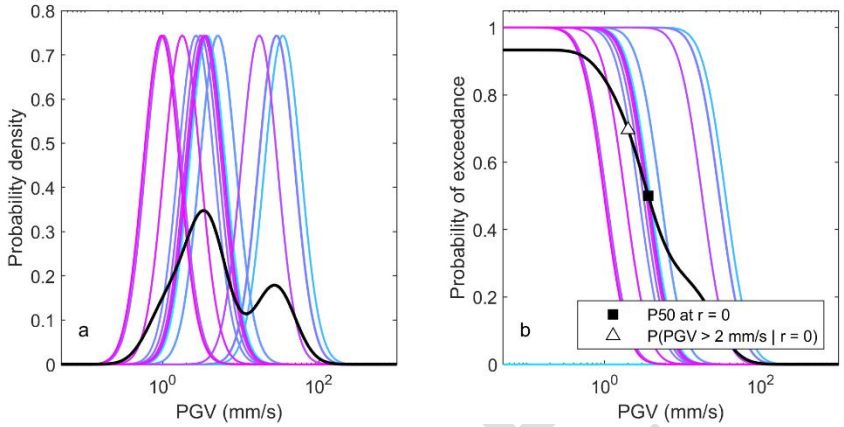

Figure 11 Synthetic example PGV distributions at the epicenter (r = 0), for 15 random magnitudes between 1.5 and 3.5 at 2 km depth. In 1 of the 15 cases, it is modelled that no seismicity has occurred. a) Probability density functions of individual magnitude realizations (coloured) and combined pdf of all model realizations (black). b) Probability of exceedance curves for all magnitude realizations (coloured) and combined curve (black).

From the summed pdf distributions, contours for a certain PGV threshold can be determined. In the example below, P10, and P50 values for the contour of a PGV of 2 mm/s are shown (Figure 12). Respective epicentral distances are 10.94 and 2.61 km. The P90 is not a number, as the probability of exceeding 2 mm/s is 0.72 in this example.

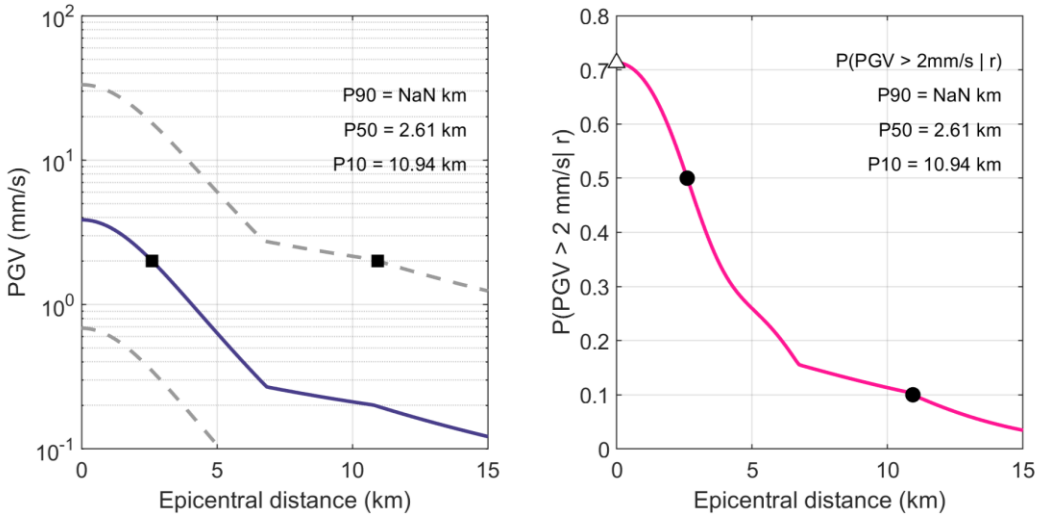

Figure 12 Contours of 2 mm/s for the same randomly picked magnitudes between 1.5 and 3.5 as shown in Figure 11. a) Contour distances of 2 mm/s shown in PGV – epicentral distance plot, for P10, P50 and P90 values. b) Probability of exceedance curve for 2 mm/s with epicentral distance, with P10, P50, and P90 values.

2.7.5. Implications of DSHA and comparison to PSHA

For DSHA the annual probability rates are not quantified, whereas for PSHA rates are accounted for (e.g. Figure 13). For the DSHA the ground motions are fully driven by the largest credible earthquake (LCE), and hence this may give a conservative approach of PGV compared to PSHA. In PSHA, another maximum earthquake is sometimes used called the Maximum Considered Earthquake, which is defined as the earthquake in a certain area with a 2 percent probability of being exceeded in 50 years. Alternatively, a maximum magnitude or maximum magnitude distribution is considered in combination with a truncation model to constrain the upper ends of the Gutenberg-Richter. In this formulation, the maximum magnitude itself will never occur with any return period; it is defined as the smallest possible magnitude, which cannot occur. However, since in a PSHA the entire frequency-magnitude distribution is taken into account, it will typically be smaller sized earthquakes which will drive the seismic hazard, since the annual rate of smaller earthquakes is much higher than that of the magnitudes approaching the largest credible earthquake magnitude. Such effects are not accounted for in the DSHA. At the moment, data on which to base earthquake rates of Gutenberg-Richter relationships near geothermal sites are not available. If sufficient frequency-magnitude data is available in the future, a more probabilistic approach may be considered.

Whereas in PSHA many possible sources, and their uncertainties in terms of depth, location, etc. are considered, in the current DSHA only one fault is considered. The epicenter location remains at the same position (i.e. the closest point on the fault to the injection well, at mid reservoir depth). Hence, uncertainty in the source location is not accounted for when constructing the PGV contours. In addition, the possibility that other faults nearby are also intersected by the cold front and get reactivated is not included. It is recommended to add the effect of multiple sources in future versions of the DSHA, as this may have a significant effect on the PGV contours.

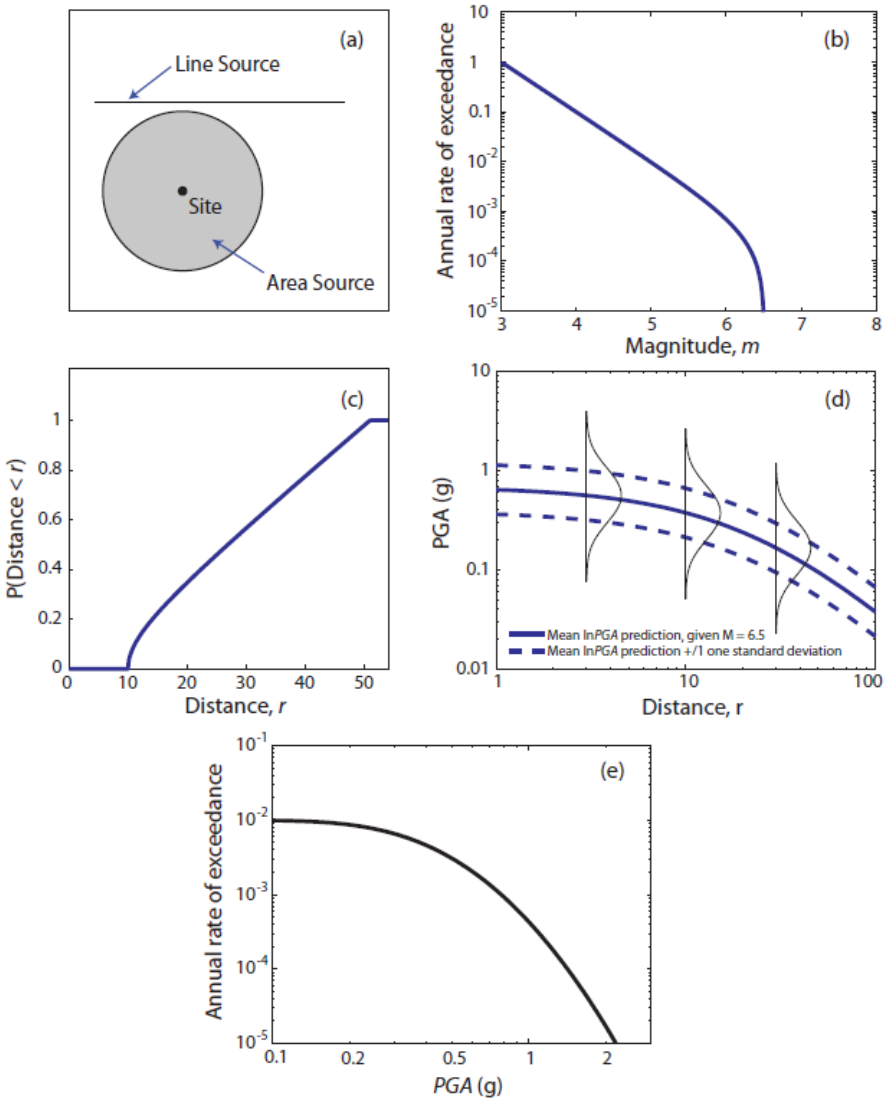

Figure 13 Typical PSHA workflow, Baker et al. (2021).

3. Validation of SRIMA calculations

3.1. Validation of the pressure and temperature calculation in SRIMA

We have validated the SRIMA-calculated temperature and pressure fields to output generated by Eclipse for the same input parameters. To this end we modelled an aquifer in which we injected cold water for a long time. The base case of the aquifer thickness of 100 m was varied: 30 m and 300 m thickness was also tested. Figure 14 and Figure 15 show good agreement between the SRIMA results and the Eclipse results. For thicker and thinner reservoirs, the agreement was the same. Only some numerical diffusion in Eclipse causes a more gradual temperature decrease in the reservoir; further, the leakage of (negative) heat to the bounding layers causes some vertical differentiation of the temperature profile in the aquifer near the thermal boundary.

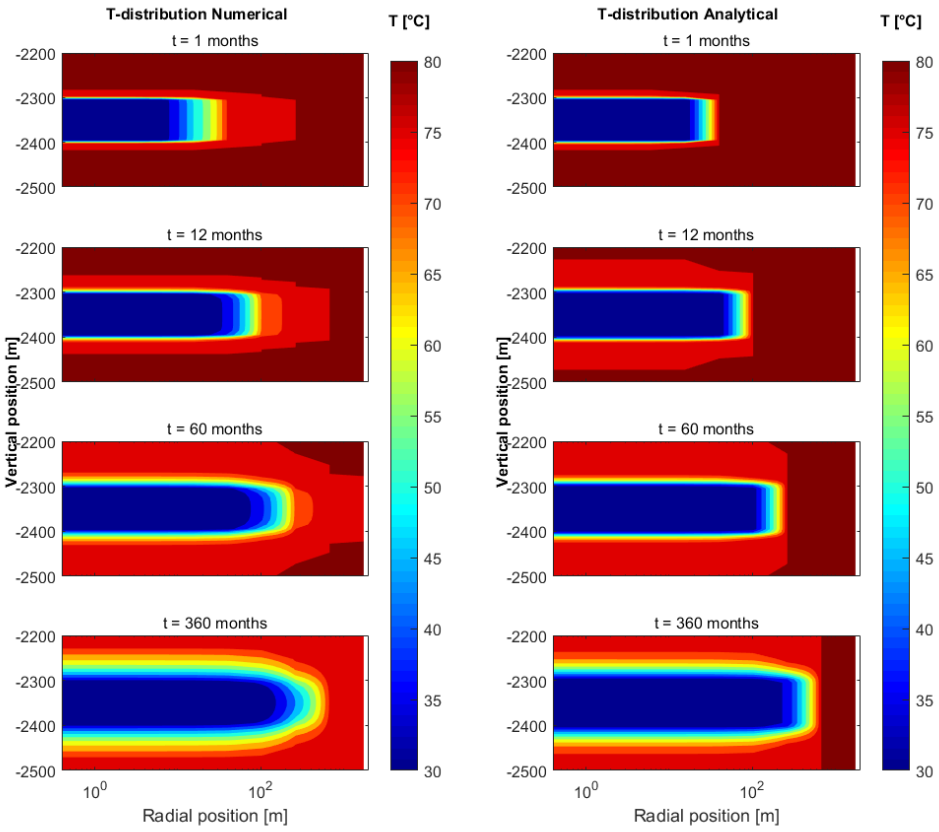

Figure 14 Contour plots of the benchmark results of the temperature correlations. Left: numerical results. Right: Analytical results with SRIMA. Note that the radial axis is spaced logarithmically

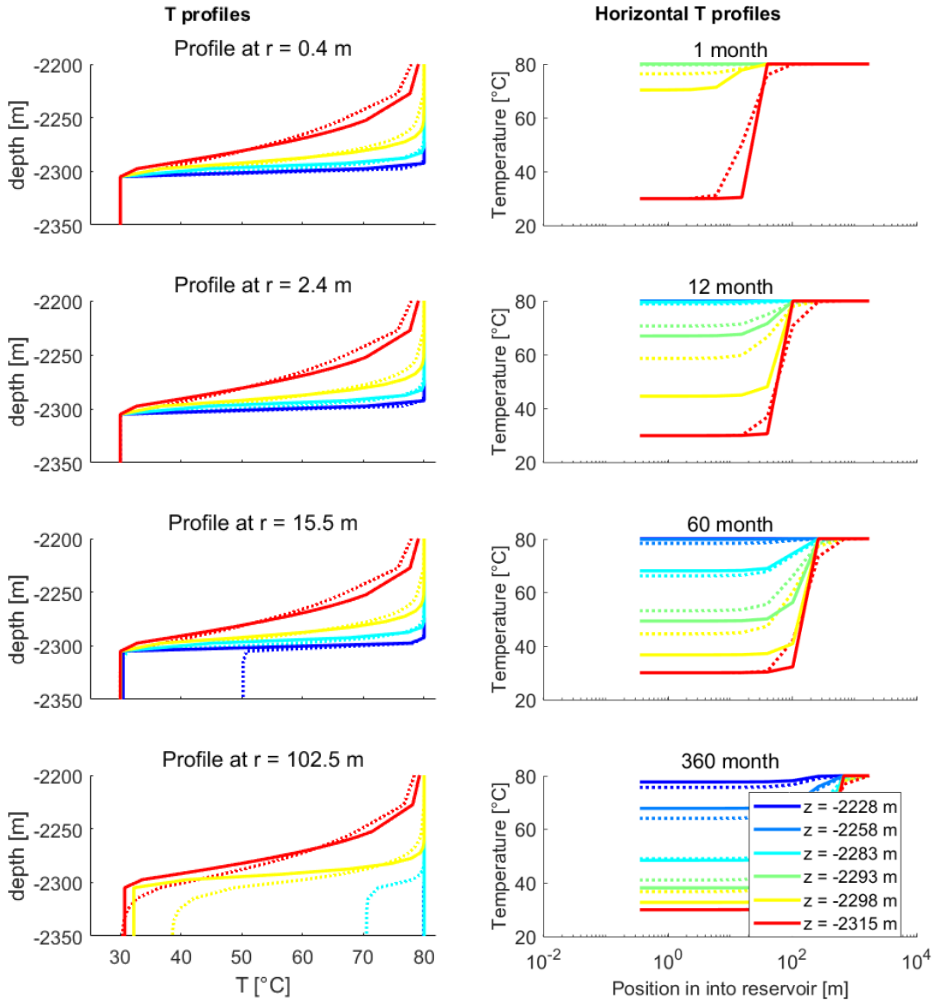

Figure 15 Line plots of the benchmark results of the temperature correlations at different distances from the well. Left: vertical profiles. Colors dark blue, light blue, yellow and red indicate timings at 1, 12, 60 and 360 months; dotted curves are numerical results and solid curves are analytical results. Right: horizontal profiles at different vertical positions and different times

The pressure response as calculated in SRIMA was also verified using Eclipse. Figure 16 and Figure 17 give the results. As expected, the pressure profiles are indeed logarithmically decreasing with the radius, with different slopes in the cold and hot zones. This is best demonstrated in the profiles along a horizontal line: the pressures in the reservoir (red lines in right plot of Figure 17) show a change in slope at the position of the cold front. Profiles for the 30-m and 300-m thick reservoir showed essentially the same behavior. The correspondence between numerical and analytical results in the bounding layers is slightly worse than for the temperature; this is mainly due to the pressure gradient present along the complete reservoir. Actually, this validation was used as a benchmark for the optimization of the choice of the effective cylinder pressure mentioned in Section 2.2.4.

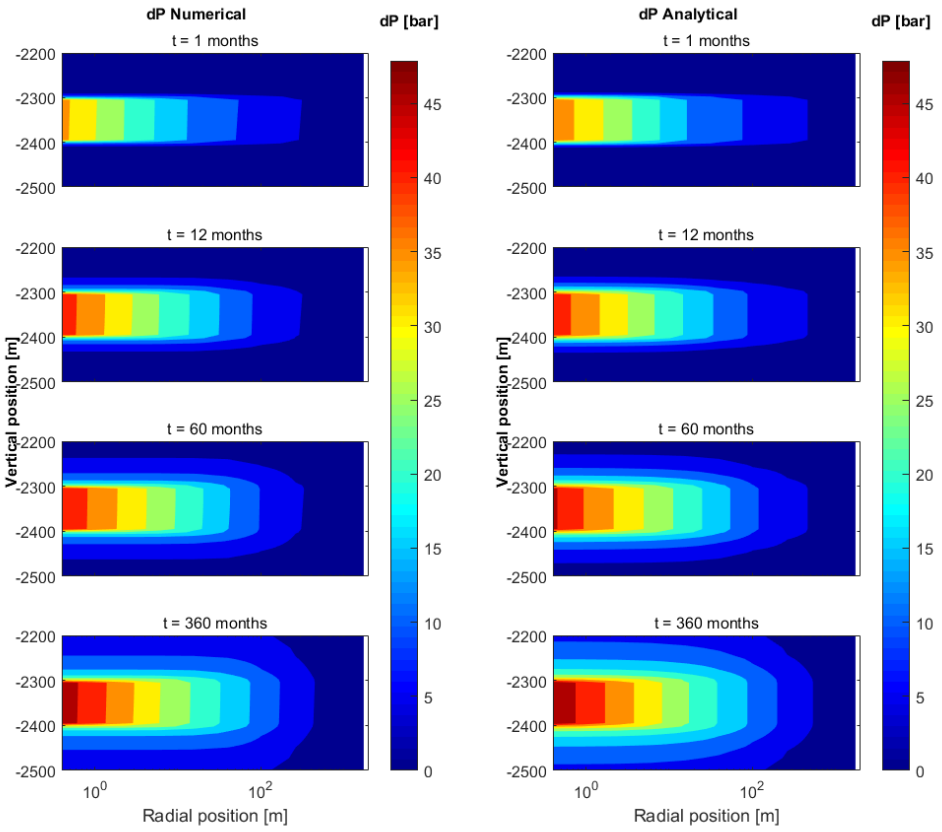

Figure 16 Contour plots of the benchmark results of the pressure correlations. Left: numerical results. Right: Analytical results with SRIMA. Note that the radial axis is spaced logarithmically.

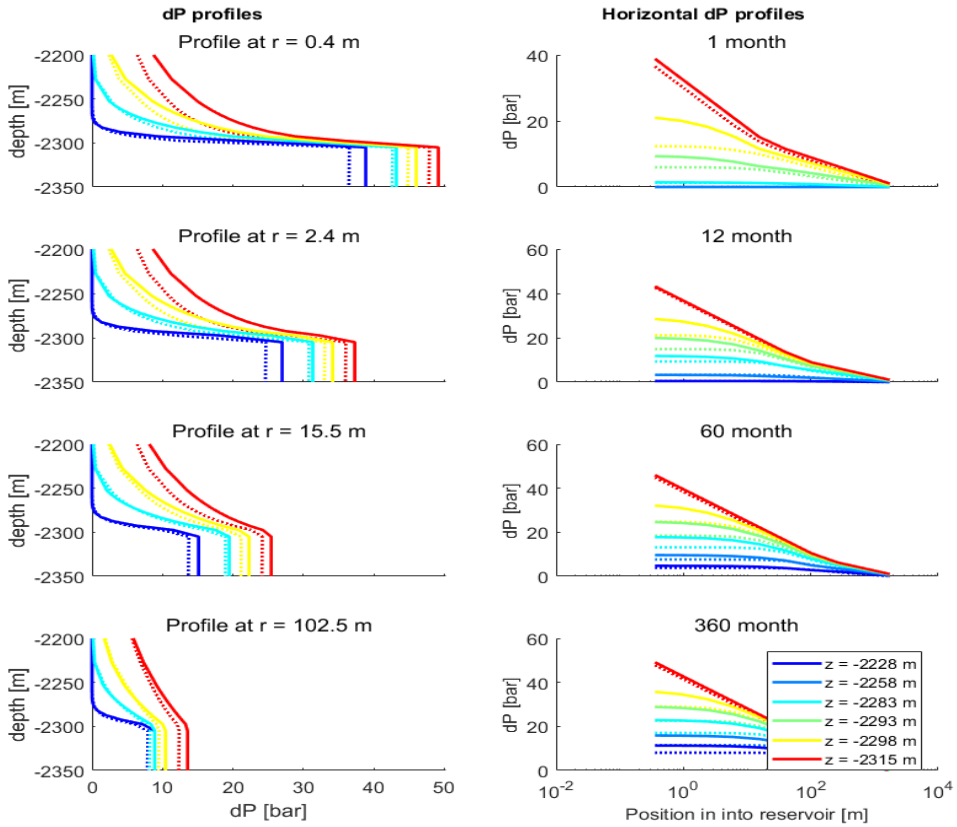

Figure 17 Line plots of the benchmark results of the pressure correlations at different distances from the well. Left: vertical profiles. Colors dark blue, light blue, yellow and red indicate timings at 1, 12, 60 and 360 months; dotted curves are numerical results and solid curves are analytical results. Right: horizontal profiles at different vertical positions and different times

3.2. Validation of stress calculation

3.2.1. Model setup and input parameters

SRIMA simulates the poro-thermo-elastic stress changes due to injection into a reservoir formation overlain by a seal formation and underlain by a base formation (Section 2.1.1). The calculation of the stress change has been benchmarked against the Finite Element software DIANA FEA. The model setup in DIANA is similar to that of SRIMA; however, whereas seal and base are assumed to have infinite height in SRIMA a free surface is included in DIANA and the model depth is finite with a maximum depth of -5000 m (Figure 18). Fixed displacement boundaries were imposed at the model sides and base, preventing displacement in the direction perpendicular to the boundary but allowing displacement parallel to the boundaries. Like in SRIMA the model width was 2500 m and the well radius 0.2 m, and the reservoir formation was situated at -2300 m with a thickness of 100 m.
The formations were modeled with linear triangular and quadrilateral elements (T6AXI and Q8AXI). The element size increased from 2 m at the well in the reservoir to a maximum of 20 m further away from the well.

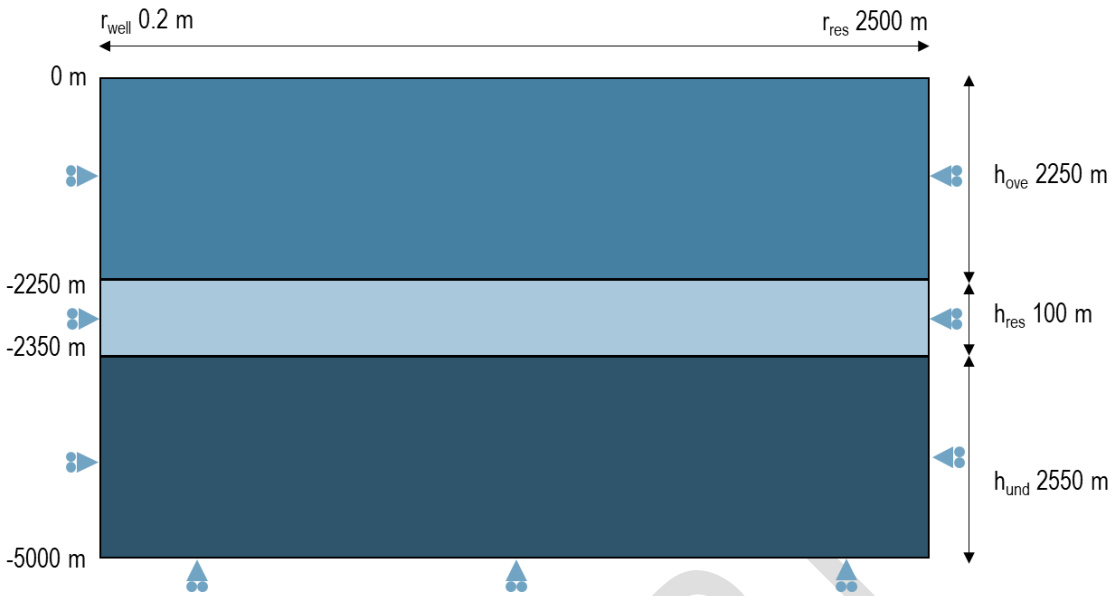

Figure 18 Axisymmetric model in DIANA used to benchmark stress calculation in SRIMA. Triangles indicate the presence of displacement boundaries preventing motion perpendicular to the boundary.

Table 1 Input parameters used for the benchmark of stress changes computed in SRIMA vs Eclipse and DIANA FEA.

Parameter (DIANA & SRIMA)	Symbol	Unit	Value
Mid depth	y_{mid}	m	**2300**
Reservoir thickness	h	m	**100 (30, 300)**
Throw	t	m	**NA**
Dip	θ	°	**70**
Vertical stress gradient	$\Delta\sigma_v/\Delta y$	Mpa/km	**22.6**
Stress ratio σ_h / σ_v	K_0	-	**0.708**
Horizontal stress ratio σH / σh	σ_H / σ_h	-	**1**
Pressure gradient	$\Delta\sigma_v/\Delta y$	Mpa/km	**10.72**
Strike with respect to σ_H	φ	deg	**0**
Overpressure in the reservoir	P_{exc}	Mpa	**0**
Biot coefficient	α	-	**1**
Poisson's ratio	v	-	**0.1**
Young's modulus	E	Gpa	**15 (3.75, 60)**
Linear thermal expansion coefficient	η	$°C^{-1}$	**$1.20 \cdot 10^{-5}$**
Static friction	f_s	-	**0.6**
Flow-Temp parameters (Eclipse & SRIMA)			
Permeability	k	mD	**500**
Overburden permeability	k_{seal}	mD	**$3.0 \cdot 10^{-5}$**
Reservoir temperature	T_{res}	°C	**80**
Injection temperature	T_{inj}	°C	**35**
Thermal conductivity	K_{rock}	W/mK	**3.50**
Specific heat capacity water	c_{fluid}	J/kgK	**4200**
Specific heat capacity rock	c_{rock}	J/kgK	**850**
Seal density	ρ_{rock}	kg/m3	**2200**
Seal porosity	ϕ_{seal}	-	**0.1**
Seal Poisson ratio	v_{seal}	-	**0.1**
Density water	ρ_w	kg/m3	**1000**
Mass injection rate	q	kg/s	**50**
Water viscosity at T0	μ_c	Pas	**0.0003**
Water viscosity at Tinj	μ_h	Pas	**0.001**
Total compressibility	c	1/Pa	**$4.0 \cdot 10^{-10}$**

For the validation of the induced stresses, pressures and temperatures were computed in SRIMA. This PT-field was used as an input in DIANA, so both SRIMA and DIANA started with the same PT-changes from which the poro-thermo-elastic stresses are computed. The PT-field was computed at the node locations of the DIANA mesh. The PT-field after 30 years of injection was used for the benchmark. Note that rather than a temperature gradient as used in Chapter 5 a constant initial temperature of 80 degrees was assumed for the reservoir and seal and base formations.

In the benchmark exercise we compared both the horizontal, vertical and shear stress, as well as the Coulomb Stress Changes which are important for fault reactivation. Coulomb Stress Changes (CSC) are calculated as

$$CSC = \Delta\tau - \mu\Delta\sigma_n' \quad (27)$$

Where $\Delta\tau$ is the shear stress change, $\Delta\sigma_n'$ is the effective normal stress change on the fault, and μ is the static friction coefficient. For the Coulomb Stress Change a fault dip of 70° was used and a friction coefficient of 0.6.

3.2.2. *Stress changes – Uniform elasticity*

Figure 19 shows the horizontal and vertical stress changes modeled in DIANA and SRIMA after 30 years of injection, and Figure 20 shows the shear, normal, and Coulomb stress changes for a fault dip of 70°. The cooling front extends for 570m from the wellbore, which is clearly reflected in the stress changes; the largest stress changes occur within the cooled volume. Since the pressure changes are small the poro-elastic response is limited and the stress response is dominated by thermo-elastic stress changes. The stress response to injection can be summarized as following:

- A decrease in total horizontal stress in the cooled volume, of 8.1 MPa for the current model. This is slightly less than the horizontal stress decrease for the same amount of cooling (ΔT = -45°) for a laterally extensive reservoir, which is given by $\Delta\sigma_{x(laterally\ extensive)} = \gamma_T \Delta T$ = -9 MPa (Figure 19).
- A decrease in total vertical stress in the cooled volume. This decrease is much smaller than the horizontal stress decrease, with a maximum decrease of -2 MPa (Figure 19).
- The largest shear stress changes occur at the outer edges of the cooled front (Figure 19).
- The Coulomb Stress Change is largest within the cooled volume (Figure 20, Figure 21). The positive values of the CSC indicates the stress becomes more critical for the typical normal faulting orientation considered here.

Vertically oriented stress concentrations can be seen in the vertical stress changes computed in SRIMA (Figure 19, Figure 21). These stress concentrations are an artefact due to simplifications made for the analytical thermo-elastic stress calculation. The temperature field was approximated with 10 cylinders, each with a uniform temperature decrease of 10% of the total temperature decrease and a radius corresponding to 10% temperature decrease. The thermo-elastic stresses of each of these 10 cylinders can be computed analytically using the Myklestad solution, and stress changes of each cylinder are superimposed to obtain the total thermo-elastic stress changes (Section 2.2). In DIANA the thermo-elastic stress is computed directly from the temperature field and no such concentrations are seen. Furthermore, the comparison between SRIMA and DIANA FEA shows that, for uniform elasticity:

- SRIMA overestimates the horizontal stress decrease within the cooled reservoir volume by ~7% (Figure 21).
- SRIMA underestimates the vertical stress decrease within the cooled reservoir volume with ~1 MPa which is ~30-50% of the total vertical stress decrease (Figure , Figure 21). In Figure 19 the variations in vertical stress due to the approximation of the temperature with discrete cylinders as mentioned above can be seen, with abrupt changes in vertical stress of ~0.5 MPa which locally cause larger differences with respect to the DIANA results.
- SRIMA overestimates the Coulomb Stress change on a fault within the cooled reservoir volume computed by 15%, and even more in the cooled volume of the seal or base (Figure 20, Figure 21).
- SRIMA is thus conservative for fault reactivation within the cooled volume, for a normal faulting regime and relatively steep faults.
- Just to the side of the cooled volume (~600 m from the well) SRIMA underestimates the vertical stress increase and horizontal stress decrease. The resulting Coulomb stress change is underestimated by SRIMA; hence, SRIMA is not conservative just outside of the cooling front.
  Overall, the agreement between DIANA and SRIMA is reasonable (<7% difference in most of the cooled volume) and SRIMA is conservative within the cooled volume. However, just outside the cooling front SRIMA is not conservative. This should be considered for fault reactivation studies. Also, care must be taken not the consider the artificial vertical stress variations for fault reactivation.

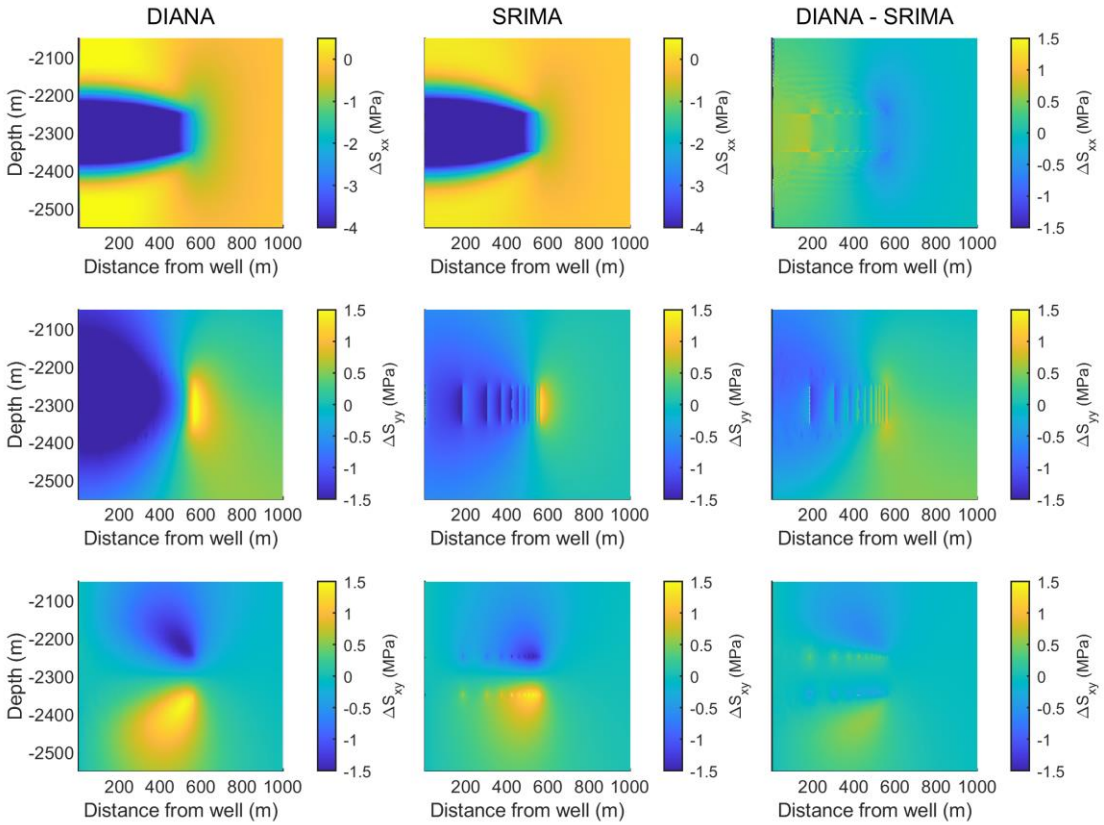

Figure 19 Stress changes modeled in DIANA and SRIMA and differences between stress changes in both models, for a uniform elastic properties. Stress changes are computed after 30 years of injection, assuming the same pressure and temperature changes for both models. Horizontal stress change: ΔS_{xx}, vertical stress change: ΔS_{yy}, and shear stress change: ΔS_{xy}. Left column shown DIANA results, and the middle column the results from SRIMA. Right column shows the difference in stress change between DIANA and SRIMA, with positive values indicating the stress computed in DIANA is larger than in SRIMA.

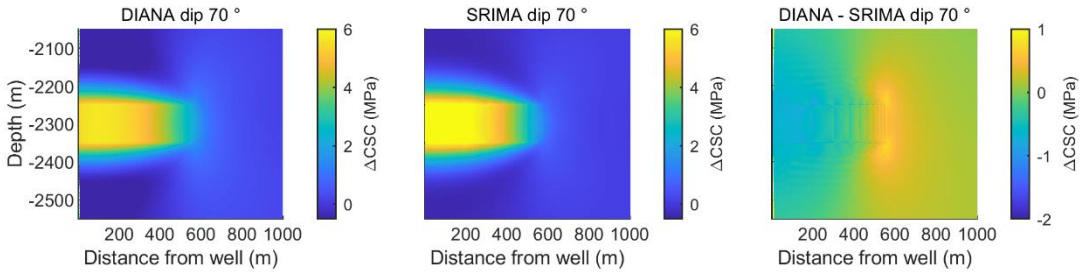

Figure 20 Coulomb Stress Changes modeled in DIANA and SRIMA and differences between stress changes in both models, for a uniform elastic properties, a dip of 70° and a friction coefficient of 0.6. Stress changes are computed after 30 years of injection.

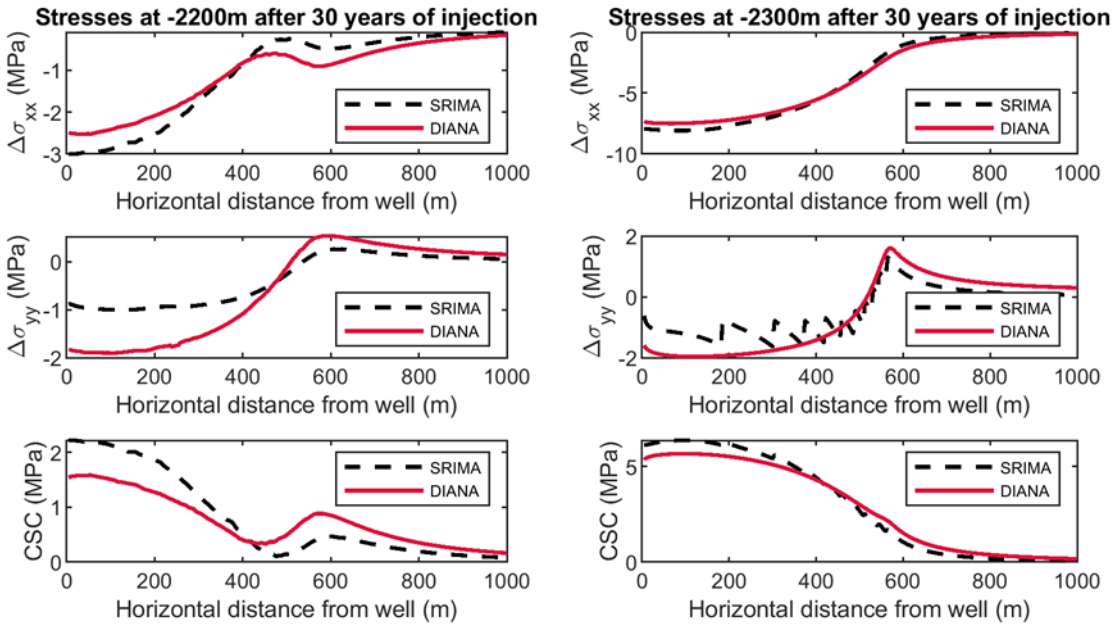

Figure 21 Comparison of horizontal and vertical stress changes and Coulomb Stress Changes computed in DIANA and SRIMA at different depths, for uniform elasticity. Lefthand side: -2200 m depth, 50 m up into the seal formation. Righthand side: -2300 m depth, in the middle of the reservoir.

3.2.3. *Stress changes – Stiffer seal and base*

The poro-thermo-elastic stress changes have also been compared for heterogeneous elasticity, with seal and base formations having a 4x higher stiffness than the reservoir (Figure 22 – Figure 24). Note that this is an upper bound to stiffness contrasts, in reality it is likely less and model differences resulting from heterogeneous elasticity are also less.
The comparison between SRIMA and DIANA FEA shows that, for a 4x stiffer seal and base formation:

- The largest horizontal stress decrease and Coulomb stress increase occur in the cooled parts of the seal and base formations due to the higher stiffness.
- Within the reservoir the agreement between both the horizontal and vertical stress changes computed in DIANA and SRIMA is good (<5% difference), though artificial stress concentrations in vertical stress locally cause larger differences.
- The agreement between the stress changes within the cooled reservoir volume is better than for uniform elasticity, likely because the stiff seal and base reduce stress arching effects which is not captured in SRIMA.
- SRIMA overestimates the horizontal stress decrease in the cooled parts of the seal and base by ~15-20%
- SRIMA underestimates the vertical stress decrease above and below the cooled reservoir area by 50%
- The Coulomb stress changes (CSC) computed in the cooled reservoir volume show good agreement, but SRIMA overestimates the Coulomb stress change in the cooled parts of the seal and base by ~30%. Again, SRIMA is thus conservative in that it returns a larger CSC than DIANA.

- To the side of the cooled parts of the seal and base, SRIMA underestimates the Coulomb stress change.

The discrepancies are related to the application of analytical equations developed for a homogeneous body. The approximations made in Section 2.2.2 do not correctly incorporate stress arching in a heterogeneous subsurface.

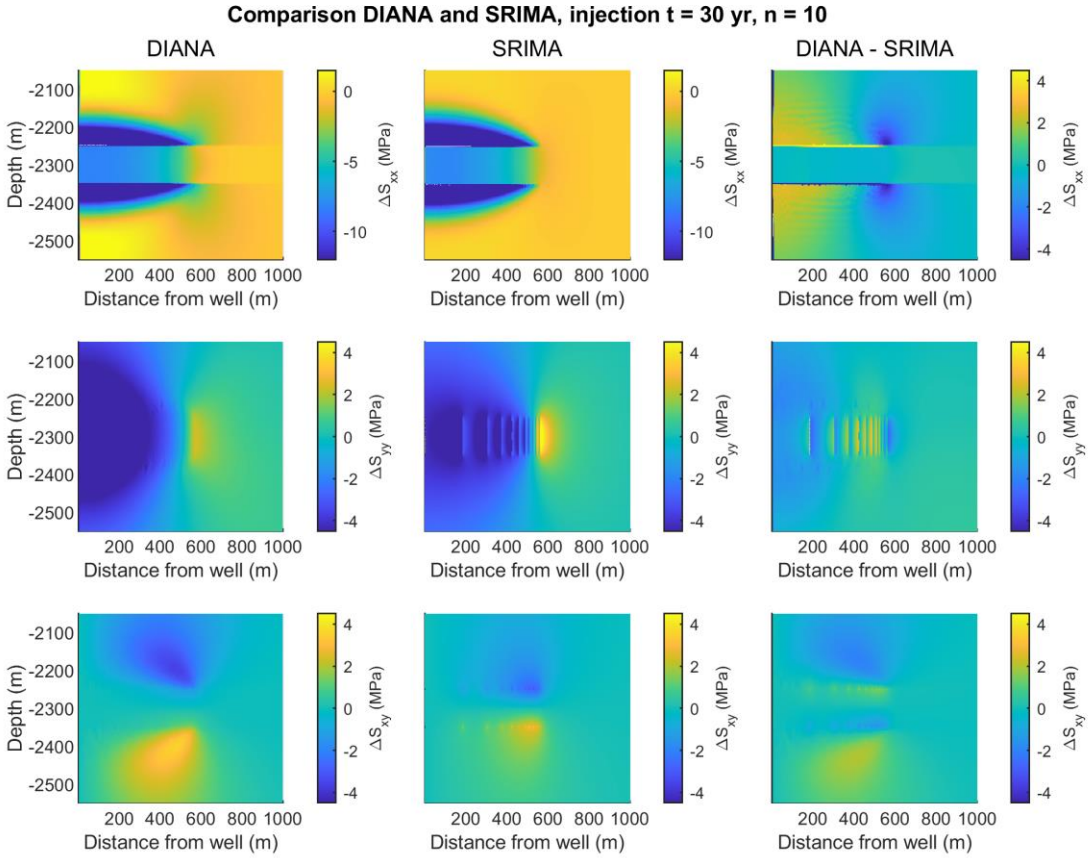

Figure 22 Stress changes modeled in DIANA and SRIMA and differences between stress changes in both models, for a 4x stiffer seal and base formation. Stress changes are computed after 30 years of injection. Horizontal stress change: ΔS_{xx}, vertical stress change: ΔS_{yy}, and shear stress change: ΔS_{xy}. Right column shows the difference in stress change between DIANA and SRIMA, with positive values indicating the stress computed in DIANA is larger than in SRIMA.

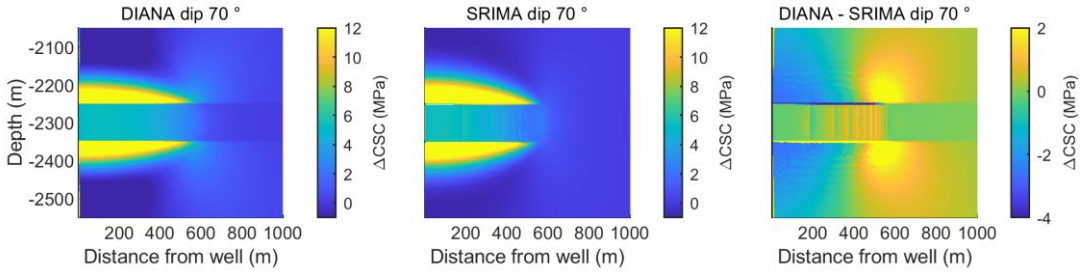

Figure 23 Coulomb stress changes modeled in DIANA and SRIMA and differences between stress changes in both models, for a 4x stiffer seal and base formation. Coulomb stress changes (ΔCSC) are computed after 30 years of injection, for a 70° dipping fault at all

locations in the model domain. Right column shows the difference in stress change between DIANA and SRIMA, with positive values indicating the Coulomb stress computed in DIANA is larger than in SRIMA.

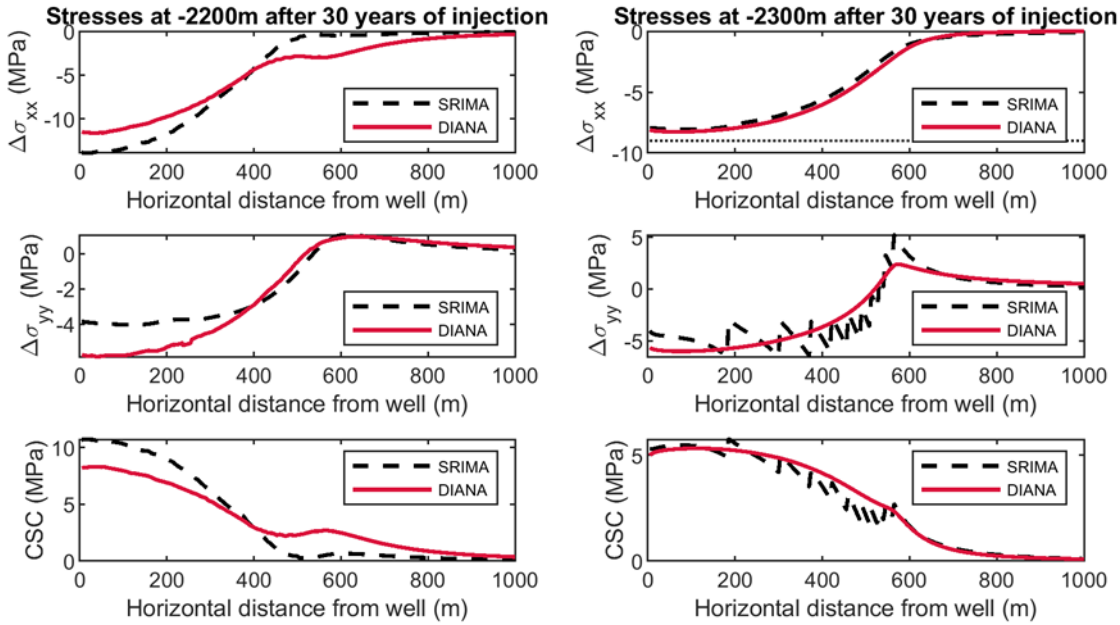

Figure 24 Comparison of horizontal and vertical stress changes and Coulomb Stress Changes computed in DIANA and SRIMA at different depths, for 4x stiffer seal and base formations. Lefthand side: -2200 m depth, 50 m up into the seal formation. Righthand side: -2300 m depth, in the middle of the reservoir.

3.2.4. *Stress changes – More compliant seal and base*

The poro-thermo-elastic stress changes have also been compared for heterogeneous elasticity, with seal and base formations having a 4x lower stiffness than the reservoir. Note that this is a significant contrast in stiffness, in reality it is likely less and differences resulting from heterogeneous elasticity are also less. The comparison between SRIMA and DIANA FEA shows that, for a 4x more compliant seal and base formation (Figure 25, Figure 26, Figure 27):

- SRIMA overestimates the horizontal stress decrease in the cooled reservoir volume by ~25% (Figure 25, Figure 27)
- SRIMA overestimates the Coulomb stress increase within the cooled reservoir volume by ~25% and is thus conservative within the cooled reservoir volume.
- SRIMA underestimates the vertical stress increase and the horizontal stress decrease to the side of the cooled reservoir volume
- SRIMA underestimates the Coulomb stress increase to the side of the cooled reservoir volume and is thus not conservative at this location.
- Stress changes outside of the cooled reservoir formation volume are significantly smaller than within the reservoir formation, but the relative mismatch between SRIMA and DIANA can be up to 100%.

Again, the discrepancies are related to the use of analytical correlations to heterogeneous subsurface for which they were not developed.

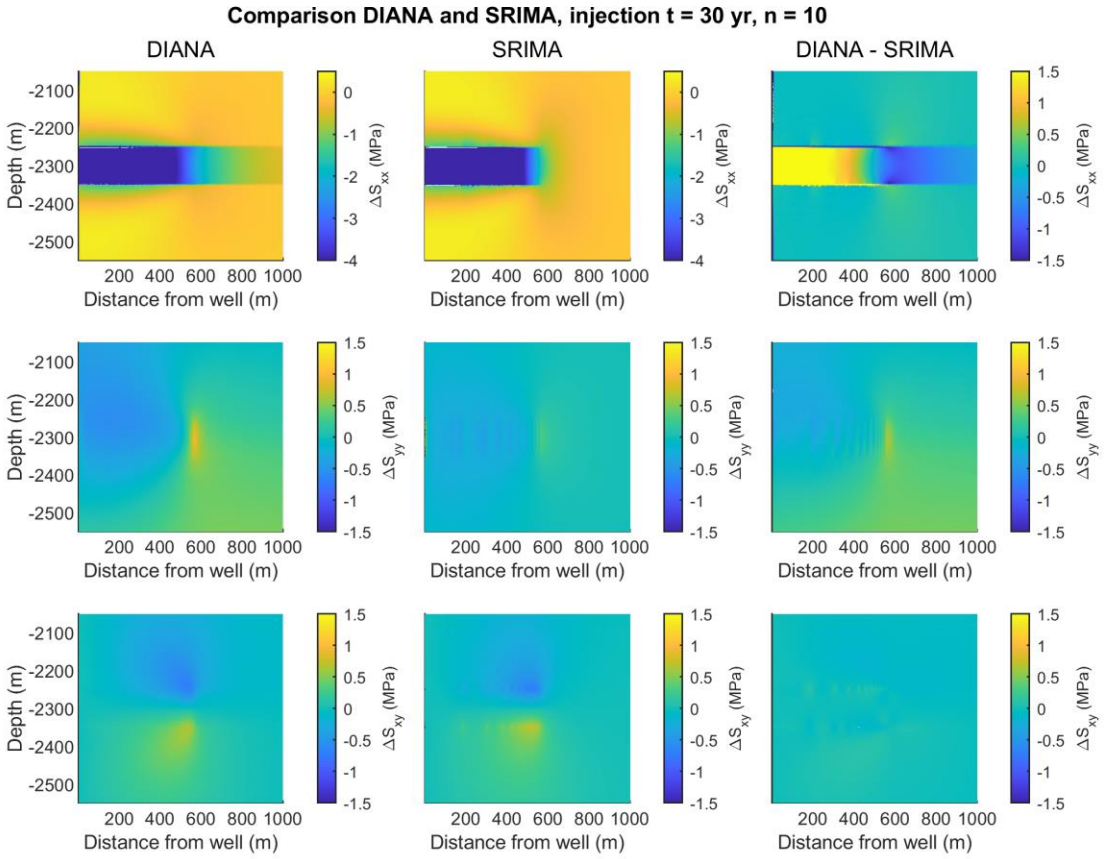

Figure 25 Stress changes modeled in DIANA and SRIMA and differences between stress changes in both models, for a 4x more compliant seal and base formation. Stress changes are computed after 30 years of injection. Horizontal stress change: ΔS_{xx}, vertical stress change: ΔS_{yy}, and shear stress change: ΔS_{xy}. Right column shows the difference in stress change between DIANA and SRIMA, with positive values indicating the stress computed in DIANA is larger than in SRIMA.

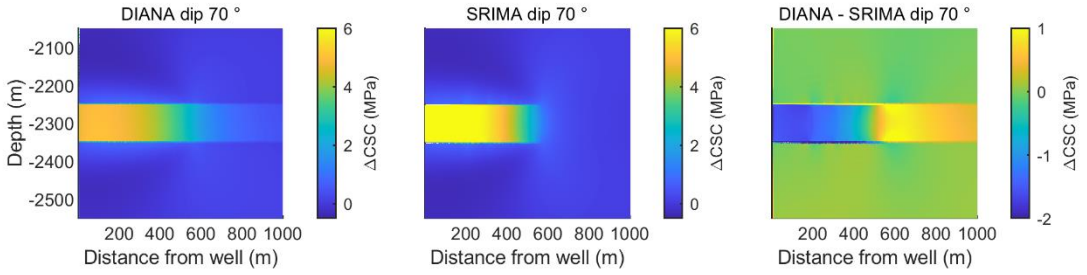

Figure 26 Coulomb stress changes modeled in DIANA and SRIMA and differences between stress changes in both models, for a 4x more compliant seal and base formation. Coulomb stress changes (ΔCSC) are computed after 30 years of injection, for a 70° dipping fault at all locations in the model domain. Right column shows the difference in stress change between DIANA and SRIMA, with positive values indicating the Coulomb stress computed in DIANA is larger than in SRIMA.

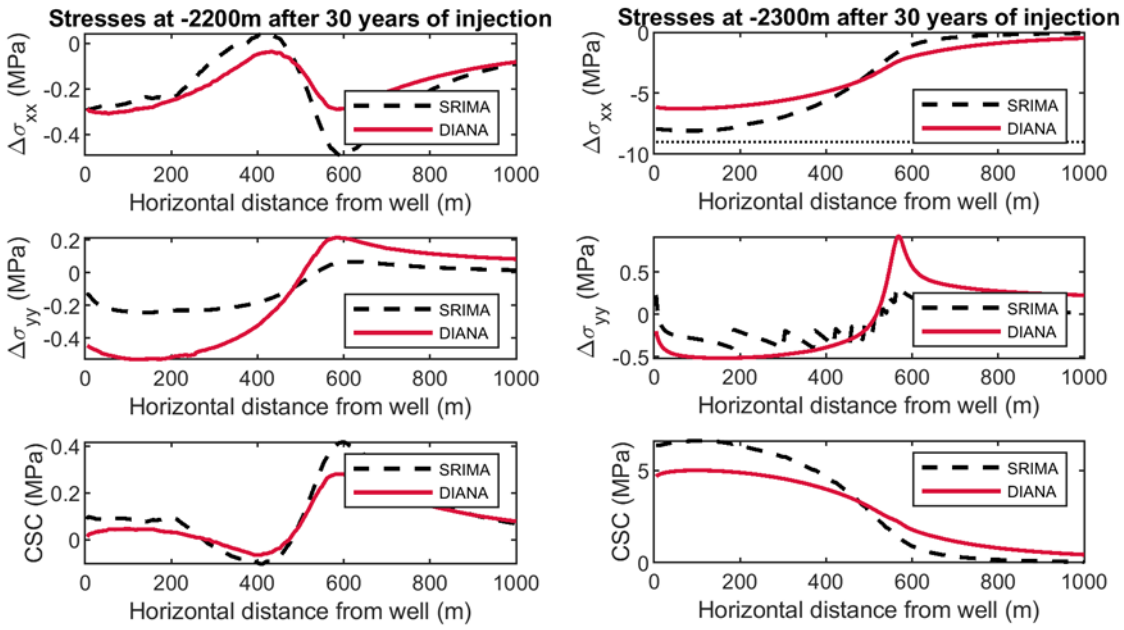

Figure 27 Comparison of horizontal and vertical stress changes and Coulomb Stress Changes computed in DIANA and SRIMA at different depths, for 4x more compliant seal and base formations. Lefthand side: -2200 m depth, 50 m up into the seal formation. Righthand side: -2300 m depth, in the middle of the reservoir.

3.3. *Effect of fault offset on stress changes*

The effect of reservoir offset along the virtual fault in the model is ignored in SRIMA. However, in previous studies of induced stress changes it was shown that stress concentrations formed on a fault when the reservoir compartments were offset along that fault (Mulders, 2003, Van den Bogert, 2015, Buijze et al., 2019, Jansen et al., 2019). These stress concentrations lead to a locally increased SCU and hence promote fault reactivation. In this section we discuss how ignoring fault offset in SRIMA would affect the modelled SCU and largest credible earthquake magnitude.

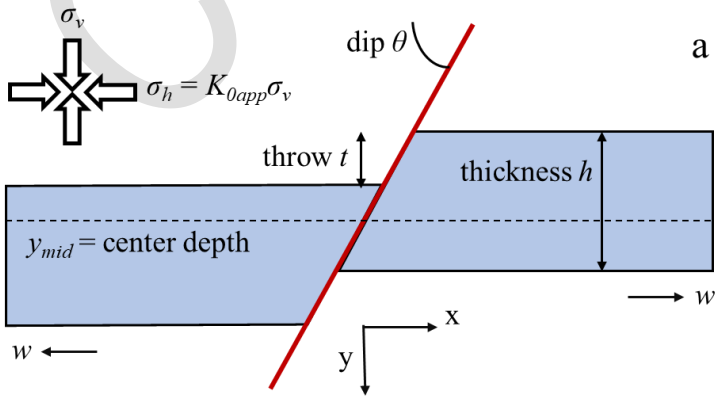

Figure 28 Plane-strain model geometry of offset reservoir compartments

Most prior studies studying the effect of offset on fault reactivation were developed in the framework of depleting gas fields (Mulders, 2003, Orlic et al., 2013, Van den Bogert, 2015, Buijze et al., 2019, Jansen et al., 2019). Therefore, a plane-strain model geometry is often assumed instead of the radial symmetric geometry used in this study. Furthermore, a simplified pressure function was often prescribed; with a uniform pressure drop within the reservoir and no pressure change outside of the reservoir. Analytical equations were derived for the stress changes within and around this offset reservoir geometry (Jansen et al., 2019), which allow for fast and convenient modelling of stress changes and fault reactivation. The nature of the model geometry and this assumed pressure profile leads to positive and negative stress concentrations (singularities in fact) in shear stress on the fault, at the top and base of the hanging wall and footwall compartments. These singularities are artificial, and the magnitude of the stress concentrations depends on the element size with which the singularity is resolved. Even so, also at the center of the reservoir, away from the singularities the offset reservoir geometry leads to an increased shear stress and SCU.

3.3.1. *Temperature (and pressure) diffusion smooths stress concentrations on offset faults*

In a recent study, the analytical equations of Jansen et al. (2019) were adapted for temperature changes (Buijze et al., 2021), in PANTHER (Physics-based Analytical Tool for Human-Induced Earthquake Rupture). In PANTHER, also the effect of temperature diffusion was accounted for in a simplified manner. It was shown that taking into account temperature diffusion (or pressure diffusion) to the seal and base tends to greatly smooths the stress concentrations, and has a large effect on the fault reactivation potential. In Figure 29 typical stress profiles are shown for a case where diffusion is not accounted for, for different offsets. The stress concentrations are clearly visible at the reservoir corners. In Figure 30 on the other hand temperature diffusion is modelled, which results in a much smoother stress profile along the fault.

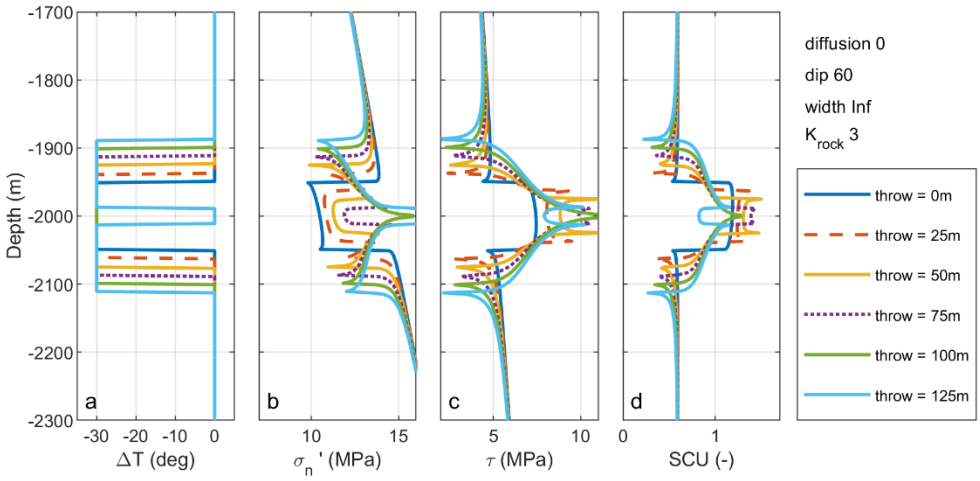

Figure 29 Example of fault stresses computed for a 30 degree temperature drop a 2D plane-strain reservoir, without temperature diffusion to the seal and base. Mid reservoir depth is 2000 m, and reservoir thickness is 100 m.

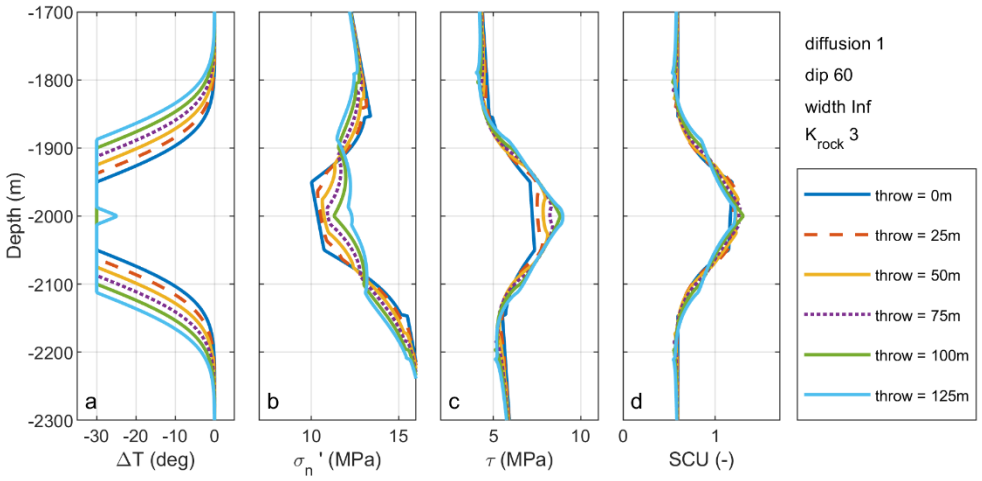

Figure 30 Example fault stresses for a 30 degree temperature drop in a 2D plane-strain reservoir, with temperature diffusion to the seal and base. Mid reservoir depth is 2000 m, and reservoir thickness is 100 m.

Accounting for temperature diffusion reduces the effect of reservoir offset on the fault stresses and SCU. Still, the offset geometry affects the effective normal stress and shear stress. The effective normal stress reduction becomes less with offset, and becomes more focused on the reservoir-reservoir juxtaposition (mid reservoir depth) y_{mid} (Figure 30b). The maximum shear stress increases with offset, with the shear stress function also becoming more focused at y_{mid} (Figure 30c). The net effect however, represented by the SCU, only shows minor differences with varying offset. Therefore it is expected that for the current example, the effect of offset on the along-dip width of the slip zone (see Section 2.7.2) is limited.

3.3.2. *Effect of dip on the impact of offset on SCU*

Note however that the SCU will vary with fault dip. For a steeper fault of 70° offset will result in a more peaked, higher SCU (Figure 31d). The difference is mainly seen around y_{mid}, and disappears at the reservoir edges. In this case, offset will tend lead .to earlier reactivation than a case without offset. However, it is likely the along-dip slip zone width is not affected much, except in the early stages of reactivation. In particular when offset remains < 0.5 the reservoir thickness the difference is not that large.

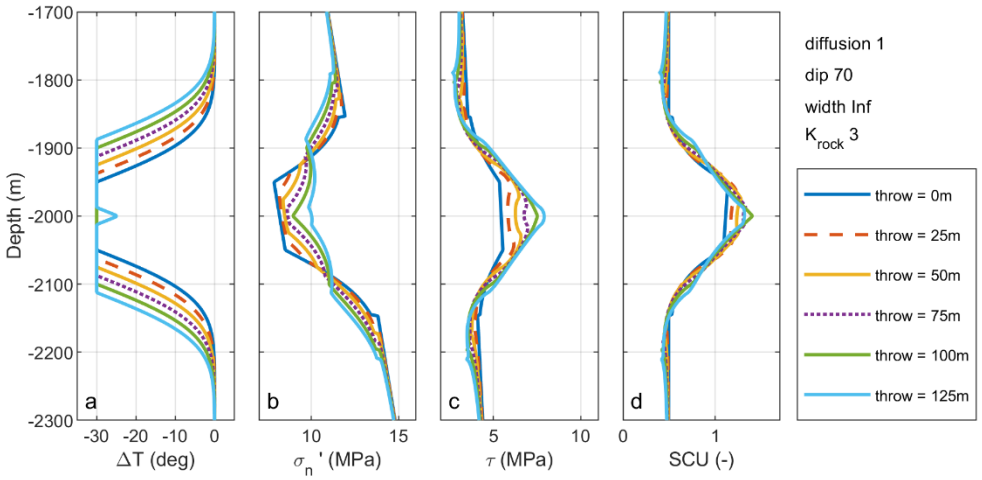

Figure 31 Example fault stresses for a 30 degree temperature drop in a 2D plane-strain reservoir, with temperature diffusion to the seal and base. Mid reservoir depth is 2000 m, and reservoir thickness is 100 m. Here the fault dip is 70°.

The steeper the dip, the larger will be the effect of offset on the SCU; see e.g. the stress development on a 90° fault (Figure 32). For very shallow dips the effect of offset on the SCU is small (Figure 33).

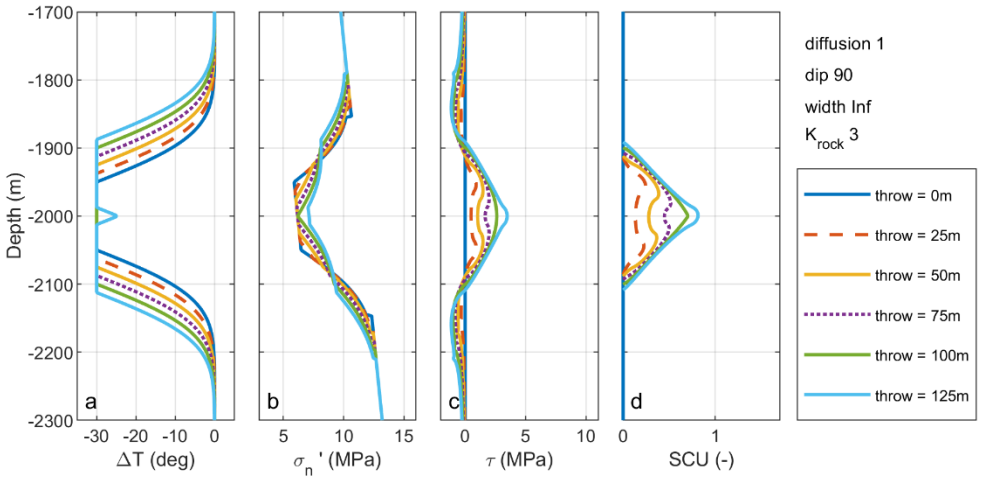

Figure 32 Example fault stresses for a 30 degree temperature drop in a 2D plane-strain reservoir, with temperature diffusion to the seal and base. Mid reservoir depth is 2000 m, and reservoir thickness is 100 m. Here the fault dip is 90°.

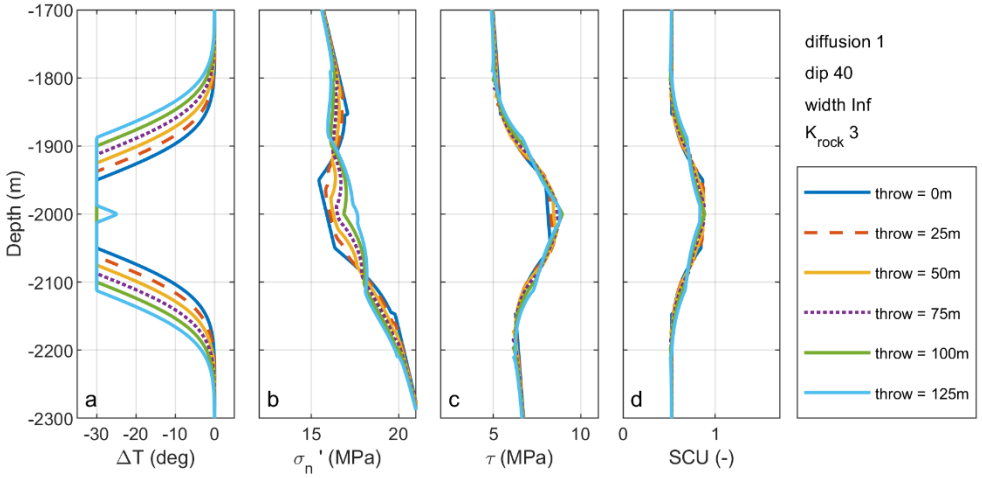

Figure 33 Example fault stresses for a 30 degree temperature drop in a 2D plane-strain reservoir, with temperature diffusion to the seal and base. Mid reservoir depth is 2000 m, and reservoir thickness is 100 m. Here the fault dip is 40°.

3.3.3. *Plane-strain vs axisymmetric*

The above model results are for a plane-strain model geometry. Cooling around an injection well is better represented by a radially-symmetric geometry, as is assumed in SRIMA. 3D modelling of stress changes on a fault offsetting two reservoir

compartments showed limited effect of reservoir offset on the Coulomb Failure Function, a variable related to the SCU (Buijze et al., 2021). However, it is noted that a single dip has been evaluated in this model (70°), and the effects of offset are apparent for the normal stress and the shear stress individually. It is recommended to extend the 3D modelling analysis to assess the effect of offset on SCU and along-dip slip zone length, for different, steeper dips, which were observed to be important in the 2D model analysis in section 3.3.2.

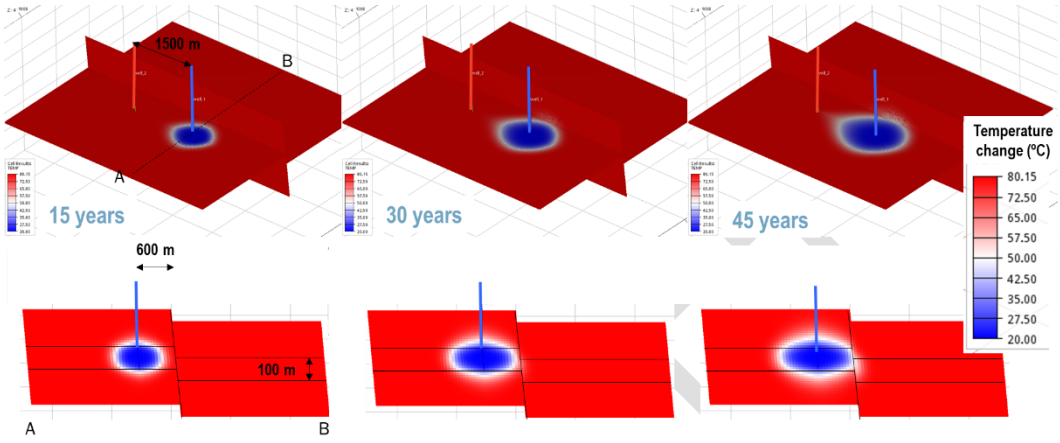

Figure 34 3D OPM Flow simulations of cooling in a reservoir offset by a fault.

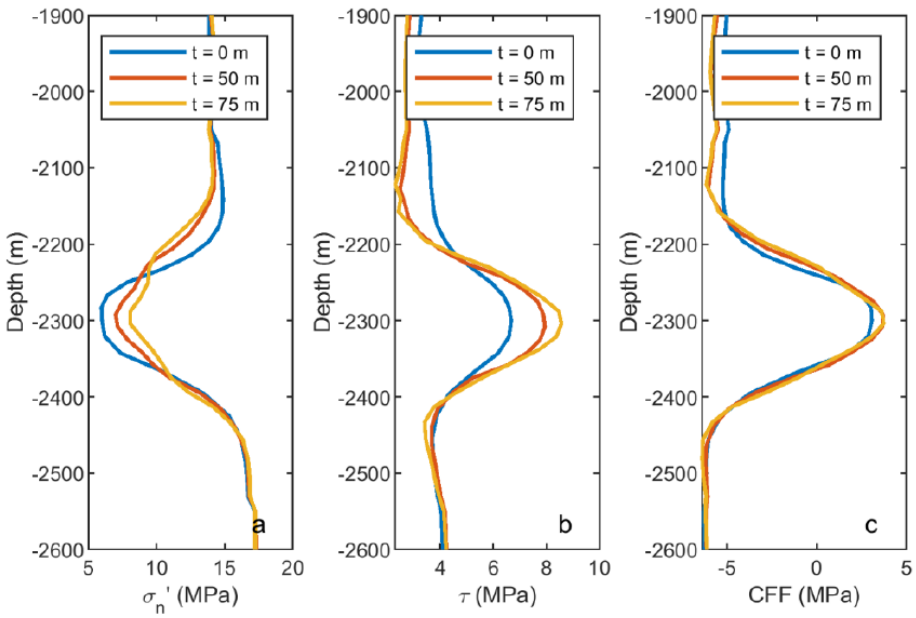

Figure 35 Effect of offset on fault stress changes, computed for a 3D flow model (OPM Flow) coupled to DIANA Finite Element Analysis. CFF: Coulomb Failure Function, where CFF > 0 indicates failure. CFF = $\tau - (\sigma_n \mu + C)$

4. Concluding Remarks

We have developed expressions for the fast calculation of temperatures, pressures, and induced poro-elastic and thermo-elastic stresses as a result of the injection of relatively cold fluid. The expressions have been benchmarked and validated by means of numerical tools. The approximations made are acceptable in the context of the uncertainty of the subsurface parameters. A stochastic implementation enables the determination of probabilities of failure and correlation of failure with model parameters.

We have used the new expressions to build SRIMA, an analysis tool for the assessment of the risk on developing tensile stresses in an aquifer or the adjacent seal and underburden, as a proxy for tensile failure or hydraulic fracturing. SRIMA allows the quick evaluation of injection scenarios and the assessment of the effect of unknown features like elasticity contrasts or stress discontinuities. Because we limit ourselves to the assessment of hydraulic fracturing only, the sometimes large discrepancies between numerical and analytical results of the vertical stresses revealed by the benchmark can be dismissed. Hydraulic fracturing in normal-faulting and strike-slip-faulting areas is driven by the horizontal stresses.

Shear failure and fault reactivation requires an additional effort, since these depend on all the stresses and on the orientation of the faults of interest. Implementation of stress determination and assessment of possible induced seismicity enables the formulation of operational safety limits like a maximum injection pressure.

References

Aki, K. (1966). Generation and propagation of G waves from the niigate earthquake of june 16, 1964. part 2. estimation of earthquake moment, released energy, and stress-strain drop from the G wave spectrum. *Bulletin of the Earthquake Research Institute, 44*, 73-88.

Baker, J. W., Bradley, B. A., and Stafford, P. J. (2021). Seismic Hazard and Risk Analysis. Cambridge University Press, Cambridge, England.

Bakx, E., Buijze, L., & Wassing, B. B. T. (2022). *Formation, lithology and region-specific stress field in the Netherlands.* (Draft Report). Utrecht: TNO. . (Report prepared within the WarmingUp project Theme 4B)

Barends, F. (2010). Complete solution for transient heat transport in porous media, following Lauwerier's concept. Paper presented at the *SPE Annual Technical Conference and Exhibition,*

Bommer, J. J., P. J. Stafford, & M. Ntinalexis (2019), Updated emperical GMPEs for PGV from Groningen earthquakes — March 2019, NAM Study Report.

Bourne, S. J., & Oates, S. J. (2017). Extreme threshold failures within a heterogeneous elastic thin sheet and the spatial-temporal development of induced seismicity within the groningen gas field. *Journal of Geophysical Research: Solid Earth, 122*(12), 10,299-10,320. doi:10.1002/2017JB014356

Buijze, L., Van den Bogert, P., Wassing, B. B. T., & Orlic, B. (2019). Nucleation and arrest of dynamic rupture induced by reservoir depletion. *Journal of Geophysical Research: Solid Earth, 124*(4), 3620-3645.

Buijze, L., Fokker, P.A., Wassing, B., 2021. Quantification of induced seismicity potential of geothermal operations. WarmingUP, 060.43190.

Candela, T., Van der Veer, E. F., & Fokker, P. A. (2018). On the Importance of Thermo-elastic stressing in Injection-induced earthquakes. *Rock Mechanics and Rock Engineering, 51*(12), 3925-3936. doi:https://doi.org/10.1007/s00603-018-1619-6

Carslaw, H. S., & Jaeger, J. C. (1992). *Conduction of heat in solids* Clarendon press.

Dake, L. P. (1983). *Fundamentals of reservoir engineering*, Elsevier.

Dost, B., Edwards, B., & Bommer, J. (2016). *Local and moment magnitudes in the groningen field.* (Scientific Report). Assen: NAM.

Dost, B., Ruigrok, E., & Spetzler, J. (2017). Development of seismicity and probabilistic hazard assessment for the groningen gas field. *Netherlands Journal of Geosciences, 96*(5), s235-s245.

Fjaer, E., Holt, R. M., Horsrud, P., Raaen, A. M., & Risnes, R. (2008). *Petroleum related rock mechanics* (2nd Edition ed.) Elsevier.

Geertsma, J. (1957). A remark on the analogy between thermoelasticity and the elasticity of saturated porous media. *Journal of the Mechanics and Physics of Solids, 6*(1), 13-16.

Geertsma, J. (1973). Land subsidence above compacting oil and gas reservoirs. *Journal of Petroleum Technology,* (June), 734.

Grant, M. (2013). *Geothermal reservoir engineering* Elsevier.

Hanks, T. C., & Kanamori, H. (1979). A moment magnitude scale. *Journal of Geophysical Research, 84*(85), 2348-2350.

Jansen, J., Singhal, P., & Vossepoel, F. (2019). Insights from closed-form expressions for injection-and production-induced stresses in displaced faults. Journal of Geophysical Research: Solid Earth, 124 (7), 7193-7212.

Kanamori, H., & Anderson, D. L. (1975). Theoretical basis of some empirical relations in seismology. *Bulletin of the Seismological Society of America, 65*(5), 1073.

Kirsch, C. (1898). Die theorie der elastizitat und die bedurfnisse der festigkeitslehre. *Zeitschrift Des Vereines Deutscher Ingenieure, 42*, 797-807.

Mijnlieff, H., De Vries, S., Jaarsma, B., Vogelaar, B., Buijze, L. (2023). Seismic Hazard and Risk Assessment for geothermal projects in The Netherlands.

Mossop, A. (2001). *Injection Induced Seismicity: A Thermoelastic Model*, Ph.D. thesis, chapter 5, Stanford University.

Mulders, F. M. M. (2003). Modelling of stress development and fault slip in and around a producing gas reservoir. (Doctoral Thesis, Technical University of Delft)

Myklestad, N. O. (1942). Two problems of thermal stress in the infinite solid. *Journal of Applied Mechanics,* , A-136-A-143.

Nield, D. A., & Bejan, A. (2006). *Convection in porous media* Springer.

Orlic, B., & Wassing, B. B. T. (2013). A Study of Stress Change and Fault Slip in Producing Gas Reservoirs Overlain by Elastic and Viscoelastic Caprocks. Rock Mechanics and Rock Engineering, 46 (3), 421-435.

Perkins, T. K., & Gonzalez, J. A. (1985). The effect of thermoelastic stresses on injection well fracturing. *Society of Petroleum Engineers Journal, 25*(1), 78-88. doi:https://doi.org/10.2118/11332-PA

Ruigrok & Dost (2022). Advice on the computation of peak-ground-velocity confidence regions for events in gas fields other than the Groningen gas field. Technical report: TR-386/

SodM. (2016). *Methodiek voor risicoanalyse omtrent geïnduceerde bevingen voor gaswining - tijdelijke leidraad voor adressering MBB.* (No. VERSIE 1.2). Den Haag: State Supervision of Mines.

Starr, A. T. (1928). Slip in a crystal and rupture in a solid due to shear. *Mathematical Proceedings of the Cambridge Philosophical Society, 24*(04), 489-500.

TNO. (2020). *Probabilistic seismic hazard and risk analysis in the TNO model chain Groningen.* (No. TNO2020 R11052). Utrecht, the Netherlands: TNO. doi:https://kemprogramma.nl/file/download/57979610/tno2020-r11052-wvd-pshra-tno-model-chain-groningen-gelakt.pdf

Van den Bogert, P. A. J. (2015). Impact of various modelling options on the onset of fault slip and fault slip response using 2-dimensional Finite-Element modelling. Restricted , Report No. SR.15.11455, Rijswijk: Shell Global Solutions International B.V.

Wang, Y., & Dusseault, M. B. (2003). A coupled conductive–convective thermo-poroelastic solution and implications for wellbore stability. *Journal of Petroleum Science and Engineering, 38*(3-4), 187-198.